

# Characterization of fibril dynamics on three timescales by solid-state NMR

**Journal Article****Author(s):**

Smith, Albert A.; Testori, Emilie; Cadalbert, Riccardo; Meier, Beat H.; [Ernst, Matthias](#) 

**Publication date:**

2016-08

**Permanent link:**

<https://doi.org/10.3929/ethz-b-000119046>

**Rights / license:**

[In Copyright - Non-Commercial Use Permitted](#)

**Originally published in:**

Journal of Biomolecular NMR 65(3), <https://doi.org/10.1007/s10858-016-0047-8>

**Funding acknowledgement:**

146757 - NMR studies in the Solid State (SNF)

# Characterization of Fibril Dynamics on Three Timescales by Solid-State NMR

Albert A. Smith, Emilie Testori, Riccardo Cadalbert, Beat H. Meier,\* Matthias Ernst\*

*ETH Zürich, Physical Chemistry, Vladimir-Prelog-Weg 2, 8093 Zürich, Switzerland*

B.M.: beme@ethz.ch, +41 44 6324401

M.E.: maer@ethz.ch, +41 44 6324366

## Abstract

A multi-timescale analysis of the backbone dynamics of HET-s (218-289) fibrils is described based on multiple site-specific  $R_1$  and  $R_{1\rho}$  data sets and  $S^2$  measurements via REDOR for most backbone  $^{15}\text{N}$  and  $^{13}\text{C}\alpha$  nuclei.  $^{15}\text{N}$  and  $^{13}\text{C}\alpha$  data are fitted with motions at three timescales. Slow motion is found, indicating a global fibril motion. We further investigate the effect of  $^{13}\text{C}$ – $^{13}\text{C}$  transfer in measurement of  $^{13}\text{C}\alpha$   $R_1$ . Finally, we show that it is necessary to go beyond the Redfield approximation for slow motions in order to obtain accurate numerical values for  $R_{1\rho}$ .

## Keywords

solid-state NMR, magic-angle spinning, dynamics, relaxation, fibrils

## Acknowledgements

This work has been supported by the Swiss National Science Foundation (grants 200020\_146757 and 200020\_159797). We would also like to acknowledge thorough and carefully considered comments from a reviewer.

## Introduction

Obtaining atomic-resolution structures of proteins has become an important component of protein studies, in order to understand the correlation between structure and function. However, proteins exhibit motions on multiple timescales, making a static structure an incomplete picture. Molecular motion plays a critical role in the behavior of proteins: slow motions may indicate large-scale rearrangement of a protein, for example, as a result of a signaling process, or binding of substrates to enzymes. Faster motions are indicative of more localized motion, giving insight into local protein flexibility. Site-specific characterization of protein motions across multiple timescales complements atomic-resolution structure, giving information about both slow, concerted motions and fast, local motions. NMR spectroscopy is an ideal technique to study motion across many timescales; exchange spectroscopy (Jeener et al. 1979), relaxation-dispersion experiments (McConnell 1958), and spin-lattice relaxation (Allerhand et al. 1971) cover motions with correlation times from  $\sim 1$  second to  $\sim 1$  picosecond.

Site-specific analysis of protein dynamics utilizing solid-state NMR can typically provide information on up to 2-3 timescales of motion (Zinkevich et al. 2013), each characterized by a timescale and an amplitude, although in principle it is possible to use more complex analyses. To perform site-specific analysis of dynamics, the following measurements are commonly combined: 1) measurement of incompletely-averaged anisotropic interactions (typically one-bond dipolar couplings), 2) measurement of several longitudinal relaxation-rate constants (typically  $R_1$  or NOE), and 3) measurement of transverse relaxation times (typically  $R_{1\rho}$  or CSA-dipole cross-correlated cross-relaxation) (Chevelkov et al. 2007a; Krushelnitsky et al. 2010; Lewandowski et al. 2010; Skrynnikov 2007). Both  $R_1$  and  $R_{1\rho}$  measurements can be attributed to modulation of some  $^1\text{H-X}$  coupling and/or CSA of nucleus X at various timescales ( $R_1$  typically provides information for  $\tau_c < 100$  ns and  $R_{1\rho}$  for  $\tau_c > 10$  ns, see SI Figure 1), whereas incompletely averaged dipolar couplings provide the total amplitude of motion (characterized by its order parameter,  $S^2$ ) of the  $^1\text{H-X}$  coupling. Therefore, one can characterize protein dynamics by collecting some or all of these parameters site specifically and then fitting them to a dynamic model.

To date, a variety of studies have investigated dynamics information using solid-state NMR. Chevelkov et al. combined solution and solid-state NMR data to investigate nanosecond motion with the extended model-free approach (Chevelkov et al. 2007b; Clore et al. 1990). Chevelkov et al. and Schanda et al. used the extended model-free approach in solid-state

NMR, obtaining information on two timescales of motion, with correlation times in the nano- and picosecond ranges. (Chevelkov et al. 2009; Schanda et al. 2010). Zinkevich et al. pushes this approach towards its limit, using combined  $R_{1\rho}$ ,  $R_1$ , and  $S^2$  measurements for  $^1\text{H}$ - $^{15}\text{N}$  spin pairs, and fitting up to three motions to the data (amplitudes were determined for three motions, although correlation times could only be determined for two of three motions for many residues), while also considering temperature dependence to calculate the activation energy of the motions, utilizing the Arrhenius relationship (Zinkevich et al. 2013). Lamley et al. utilize measurements acquired from both  $^{15}\text{N}$  and  $^{13}\text{C}$ , and combined the data for analysis (Lamley et al. 2015). Other studies utilize only one or two of these measurements, thus allowing a characterization of motion on only a single timescale of interest. For example, Ma et al. utilize only  $R_{1\rho}$  (in this case,  $R_{1\rho}$  resulting from fluctuation of the isotropic chemical shift) for characterization of slow conformational exchange (on the order of  $2900\text{ s}^{-1}$ ) in ubiquitin (Ma et al. 2014) and Good et al. studied collective motion in Anabaena Sensory Rhodopsin using  $S^2$  of backbone dipole couplings and  $^{15}\text{N}$   $R_{1\rho}$  measurements (Good et al. 2014). Solid-state NMR data may also be utilized in conjunction with molecular-dynamics simulations, lending insight into the interpretation of experimental parameters (Lange et al. 2009; Ma et al. 2015; Mollica et al. 2012; Xue and Skrynnikov 2014).

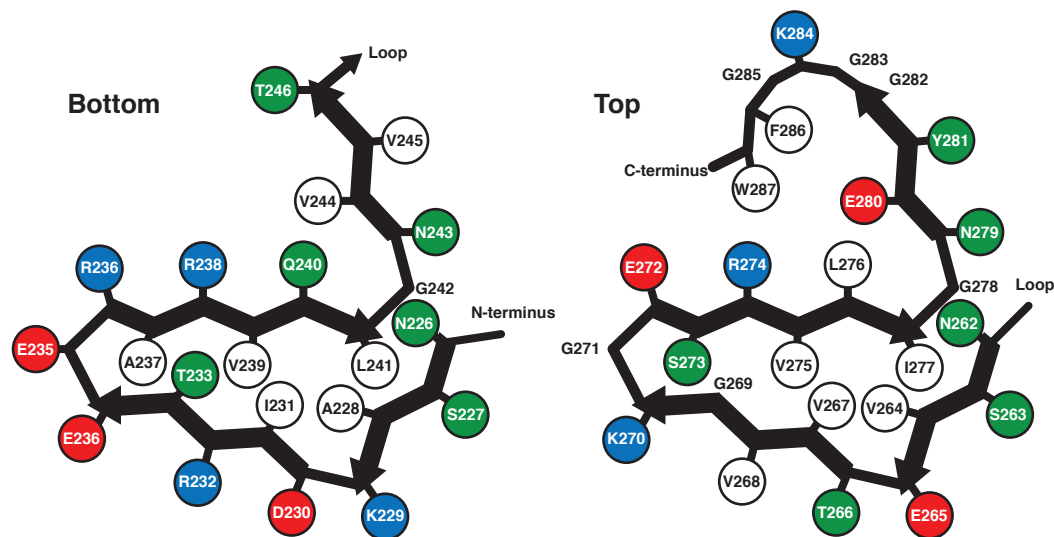


**Figure 1** Schematic representation of the HET-s (218-289) backbone structure in the context of amyloid fibrils (adapted from (Van Melckebeke et al. 2011; Wasmer et al. 2008)). Each protein monomer forms two turns of a  $\beta$  solenoid which are shown separately here, with the following color-code: white: hydrophobic, blue: positively charged, red: negatively charged, green: polar

We present a study of dynamics in the fibrils formed by HET-s (218-289), which is the prion-forming domain of the HET-s protein from *Podospora anserina*, responsible for a programmed cell death reaction, known as heterokaryon incompatibility (Glass and Kaneko 2003; Saupe 2000). HET-s (218-289) is an ideal representative for amyloid proteins, due to a high degree of local order (Siemer et al. 2006), a lack of polymorphism, and a well defined structure (Van Melckebeke et al. 2010; Wasmer et al. 2008), simplifying analysis. HET-s(218-289) is also an important model amyloid for drug design (Herrmann et al. 2015; Schütz et al. 2011). A cartoon of the HET-s (218-289) fibril structure is shown in Figure 1. We have characterized the dynamics in HET-s(218-289) fibrils using site-specific dynamics analysis of backbone  $^1\text{H}$ - $^{15}\text{N}$  and  $^1\text{H}\alpha$ - $^{13}\text{C}\alpha$  spin pairs, including measurements of  $S^2$ ,  $R_1$ , and  $R_{1\rho}$ . A more complete discussion of the biological significance of our findings will be presented elsewhere. Here, we discuss relaxation theory with particular emphasis on importance of  $^{13}\text{C}$ - $^{13}\text{C}$  transfer in  $^{13}\text{C}\alpha$   $R_1$  measurements, problems arising for measurement and calculation of  $R_{1\rho}$ , experimental methods including choice of samples and modifications to the REDOR sequence for measurement of  $^1\text{H}\alpha$ - $^{13}\text{C}\alpha$  couplings, and finally data analysis with a discussion of potential pitfalls. Although our discussion is directed by particular challenges that arose when applying dynamics analysis to HET-s (218-289) fibrils, many of the conclusions are broadly applicable to the study of proteins dynamics in general by solid-state NMR.

## 1 Theory and Practical Aspects of Relaxation Measurements

### 1.1 Summary of Relaxation Formalism

Redfield relaxation theory (Redfield 1957) lays a widely-utilized basis for calculating relaxation parameters. In solids the relaxation-rate constants depend on the orientation of individual crystallites relative to the external magnetic field, and in fact those rates will change throughout the rotor period (Torchia and Szabo 1982). This orientation and deterministic time dependence of the relaxation-rate constants makes the data evaluation more complicated than for solution-state studies. Given the limited signal-to-noise ratio of experimental relaxation-data measurements and the limited spread of the magnitude of the rate constants due to crystallite orientations, often single-exponential decays are assumed, where the rate constant of the single exponential is approximated by the average of the rate constants (Giraud et al. 2005). The Lipari-Szabo model-free approach (Lipari and Szabo 1982), gives a simple procedure to calculate the average relaxation-rate constants from model-independent order parameters ( $S^2$ )

and correlation times ( $\tau_c$ ). In this case,  $(1-S^2)$  is related to the amplitude of motion of the anisotropic interaction (usually dipole or CSA), although the exact physical interpretation of  $S^2$  is not determined without specifying a model (see SI section 1.1 for the definition of  $S^2$  for two models).

The extended model-free approach (Clare et al. 1990) gives the spectral-density function for two motions, one fast and one slow, characterized by  $S_f^2$ ,  $\tau_f$  and  $S_s^2$ ,  $\tau_s$ , respectively, as

$$J(\omega) = \frac{2}{5}(1-S_f^2)\frac{\tau_f}{1+(\omega\tau_f)^2} + \frac{2}{5}S_f^2(1-S_s^2)\frac{\tau_s}{1+(\omega\tau_s)^2}. \quad (1)$$

The effects of the two motions are cumulative, but the contributions of the slow motion are scaled by the presence of the fast motion. Here, we have assumed that the two correlation times are separated by at least one order of magnitude so that the calculation of an effective correlation time for the fast motion is not required. From the spectral density, one can calculate  $R_1$  relaxation-rate constants of spin I induced by fluctuation of a dipolar coupling as

$$R_1^{\text{IS}} = \left(\frac{\delta^{\text{IS}}}{4}\right)^2 (J(\omega_I - \omega_S) + 3J(\omega_I) + 6J(\omega_I + \omega_S)) \quad (2)$$

where  $\delta^{\text{IS}} = -2\frac{\mu_0}{4\pi}\frac{\gamma_I\gamma_S\hbar}{r_{\text{IS}}^3}$  is the anisotropy of the dipolar-coupling tensor, and  $\omega_I$  and  $\omega_S$  are the nuclear Larmor frequencies. The  $R_1$  relaxation of spin I induced by a chemical-shift anisotropy ( $\omega_I \sigma_{zz} = 2\Delta\sigma/3$ ) is given by

$$R_1^{\text{CSA}} = \frac{3}{4}(\omega_I \sigma_{zz})^2 J(\omega_I). \quad (3)$$

The total  $R_1$  relaxation-rate constant is then given by the sum

$$R_1 = R_1^{\text{IS}} + R_1^{\text{CSA}}. \quad (4)$$

Similarly, it is possible to calculate expressions for  $R_{1\rho}$ , while accounting for the effects of both MAS and the applied RF field (Haeberlen and Waugh 1969; Kurbanov et al. 2011) using

$$R_{1\rho}^{\text{IS}} = \frac{1}{2}R_1^{\text{IS}} + \left(\frac{\delta^{\text{IS}}}{4}\right)^2 \left(3J(\omega_S) + \frac{1}{3}J(\omega_1 - 2\omega_r) + \frac{2}{3}J(\omega_1 - \omega_r) + \frac{2}{3}J(\omega_1 + \omega_r) + \frac{1}{3}J(\omega_1 + 2\omega_r)\right), \quad (5)$$

$$R_{1\rho}^{\text{CSA}} = \frac{1}{2}R_1^{\text{CSA}} + \frac{1}{6}(\omega_I \sigma_{zz})^2 \left(\frac{1}{2}J(\omega_1 - 2\omega_r) + J(\omega_1 - \omega_r) + J(\omega_1 + \omega_r) + \frac{1}{2}J(\omega_1 + 2\omega_r)\right), \quad (6)$$

$$R_{1\rho} = R_{1\rho}^{\text{IS}} + R_{1\rho}^{\text{CSA}}. \quad (7)$$

Here,  $\omega_r$  and  $\omega_1$  are the MAS frequency and RF field strength (nutating frequency) applied to the I spin, respectively, assuming that RF irradiation is applied on-resonance. Note that we will discuss the validity of the  $R_{1\rho}$  equations in Section 1.3.

Measurement of multiple  $R_1$  values at different Larmor frequencies and/or  $R_{1\rho}$  values at different spinning frequencies and rf-field strengths can in some cases be sufficient to determine both the timescale ( $\tau_c$ ) and amplitude ( $S^2$ ) of a motion or even multiple motions. However, depending on the correlation time of a given motion, it may be difficult to determine these parameters accurately because their fit values can be strongly correlated. In this case, when using the model-free approach, one can determine the total  $S^2$  independent of the correlation time by directly measuring the magnitude of the incompletely-averaged dipolar coupling of the spin pair in question. In this case, the observed dipole coupling is related to  $S^2$  by its ratio to the rigid-limit dipole coupling (calculated using the vibration-averaged bond distance):

$$S^2 = \left( \delta_{\text{obs}}^{\text{IS}} / \delta_{\text{rigid}}^{\text{IS}} \right)^2 \quad (8)$$

If motions on multiple time scales are present, then the  $S^2$  determined by direct measurement of the dipolar coupling will be the product of all order parameters of the different motions acting on the dipole coupling.

$$S^2 = S_1^2 \cdot S_2^2 \cdot \dots \quad (9)$$

Note that if the timescale of a motion is slower than the recoupling rate of the experiment used to measure  $S^2$ , then this motion will not be observed via the order parameter. For a  $^1\text{H}$ - $^{13}\text{C}$  one-bond dipole coupling ( $\delta = 44.8$  kHz), this means that sensitivity of the recoupling experiment to slow motions will begin to degrade for correlation times of 10s of microseconds.

In order to utilize the above equations, one must be able to assume that the spin of interest ( $^{13}\text{C}\alpha$  or  $^{15}\text{N}$  in our case) is only affected by  $R_1$  or  $R_{1\rho}$  relaxation from the dipole coupling to the bonded  $^1\text{H}$  and its own CSA. Couplings to other nuclei are weak enough that their effect on relaxation-rate constants is usually negligible.  $R_1$  measurements can be distorted because of cross relaxation to the bonded  $^1\text{H}$ , which results in a coupled system of relaxation equations. However in solid-state NMR,  $^1\text{H}$  inversion rates, which are typically induced by proton spin diffusion, are sufficiently fast to decouple the system of equations. Proton-driven spin-diffusion (PDS) between  $^{13}\text{C}$  nuclei (Ernst and Meier 1998) does have real

potential to distort  $^{13}\text{C}\alpha$   $R_1$  measurements, and the extent of this effect remains a contentious issue in dynamics measurement in solid-state NMR.

## 1.2 $^{13}\text{C}$ Spin-Diffusion and NOE in $R_1$ Measurements

Effects of  $^{13}\text{C}$ – $^{13}\text{C}$  magnetization transfer can be investigated with an exchange model, given by

$$\frac{d}{dt} \begin{bmatrix} \langle I_{1z} \rangle \\ \langle I_{2z} \rangle \end{bmatrix} = \begin{bmatrix} -R_1^{(1)} - k & k \\ k & -R_1^{(2)} - k \end{bmatrix} \begin{bmatrix} \langle I_{1z} \rangle - M_0 \\ \langle I_{2z} \rangle - M_0 \end{bmatrix} \quad (10)$$

where  $k$  is the rate constant for exchange of longitudinal magnetization between spins 1 and 2 and  $R_1^{(1)}$  and  $R_1^{(2)}$  are the respective relaxation-rate constants (Giraud et al. 2007). The eigenvalues of the matrix give the following characteristic rate constants,

$$\lambda_{\pm} = \frac{R_1^{(1)} + R_1^{(2)}}{2} + k \pm \frac{\sqrt{(R_1^{(1)} - R_1^{(2)})^2 + 4k^2}}{2}. \quad (11)$$

Two limiting cases for magnetization exchange then arise, the first when  $2k \gg |R_1^{(1)} - R_1^{(2)}|$ , and the second with  $2k \ll |R_1^{(1)} - R_1^{(2)}|$ , with Eq. (11) simplifying to

$$\begin{aligned} 2k \gg |R_1^{(1)} - R_1^{(2)}|: \quad \lambda_+ &= \frac{R_1^{(1)} + R_1^{(2)}}{2} + 2k, & \lambda_- &= \frac{R_1^{(1)} + R_1^{(2)}}{2} \\ 2k \ll |R_1^{(1)} - R_1^{(2)}|: \quad \lambda_+ &= R_1^{(1)} + k, & \lambda_- &= R_1^{(2)} + k \end{aligned} \quad (12)$$

In the former case, magnetization on both spins 1 and 2 decays bi-exponentially, with a combination of the two  $R_1$  rates. Since the rates are averaged together, it is very difficult to determine reliable dynamics data in this situation. In the latter case, magnetization decays mono exponentially, with rates of  $R_1^{(1)} + k$  and  $R_1^{(2)} + k$ , for spin 1 and 2, respectively. Then if  $k$  is sufficiently small compared to  $R_1$ , it is possible to obtain reliable dynamics data.

It has been shown that by spinning at 60 kHz MAS, signal decay is mono exponential and coupled spins ( $\text{C}\alpha$  and  $\text{C}\beta$ ,  $\text{C}\alpha$  and  $\text{C}'$ ) show distinct relaxation rates, giving clear indication that the limit  $2k \ll |R_1^{(1)} - R_1^{(2)}|$  is well satisfied (Lewandowski et al. 2010). However, being in this limit does not necessarily require that  $R_1 \gg k$ . Investigations of the SH3 protein at 50 kHz MAS show severe changes in measured  $R_1$  relaxation rates when measuring a uniformly  $^{13}\text{C}$  labeled sample, as compared to a sample prepared such that most  $^{13}\text{C}$  have only  $^{12}\text{C}$



neighbors, using a sample grown with 2-<sup>13</sup>C glycerol (Asami et al. 2015). Larger  $R_1$  rates in the uniformly <sup>13</sup>C labeled sample are then most likely attributed to <sup>13</sup>C–<sup>13</sup>C transfer, indicating that rates measured in this sample are not very reliable for dynamics analysis.

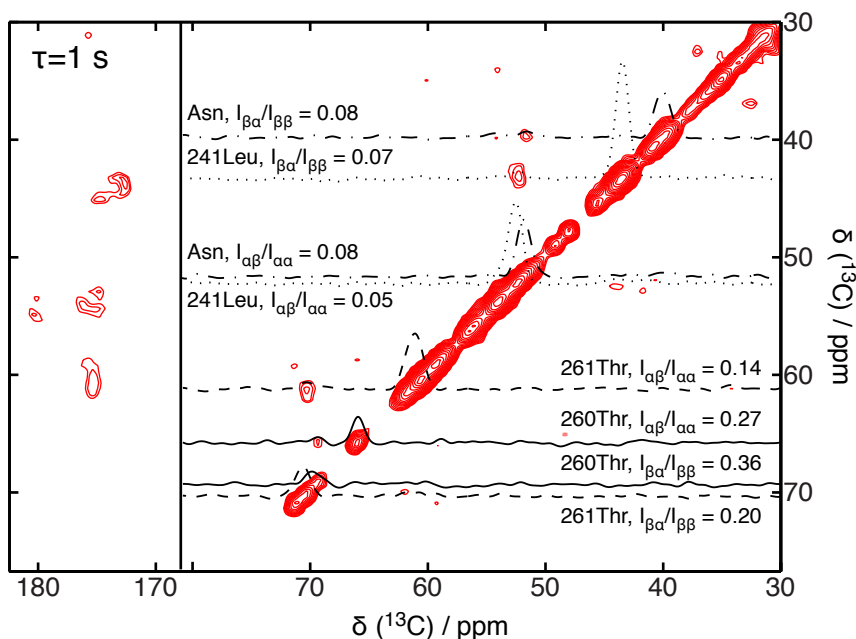


**Figure 2** <sup>13</sup>C–<sup>13</sup>C PDS spectrum with 1 s mixing. Traces are shown through the most prominent cross-peaks, and the ratio of the cross peak intensity to the diagonal peak intensity is indicated. The rate constant of magnetization transfer between the C $\alpha$  and C $\beta$  is bounded by  $(I_{\alpha\beta}/I_{\alpha\alpha}) < k_{\alpha\beta} \tau < I_{\beta\alpha}/I_{\beta\beta}$  (here,  $\tau = 1$  s). Also shown is the C $\alpha$ –CO region, where peaks resulting from <sup>13</sup>C–<sup>13</sup>C NOE transfer are visible.

We have used a partially protonated, uniformly <sup>13</sup>C labeled sample in this study for <sup>13</sup>C $\alpha$   $R_1$  measurements, and so it is critical that we verify that the rates obtained are primarily due to relaxation induced by the <sup>1</sup>H $\alpha$ –<sup>13</sup>C $\alpha$  dipole coupling and the <sup>13</sup>C $\alpha$  CSA- as opposed to <sup>13</sup>C–<sup>13</sup>C polarization transfer. It is possible to estimate the rate of spin-diffusion for a pair of <sup>13</sup>C spins from the ratio of cross-peak intensity to diagonal peak intensity in a <sup>13</sup>C PDS spectrum (Giraud et al. 2007; Lewandowski et al. 2010) and one can in fact, put bounds on the spin-diffusion rate constant. For example, for a C $\alpha$ –C $\beta$  pair, where we assume that  $R_1^\alpha < R_1^\beta$ , it can be demonstrated that  $I_{\beta\alpha}/I_{\beta\beta} \geq k_{\alpha\beta} \tau \geq I_{\alpha\beta}/I_{\alpha\alpha}$ , where  $I_{\beta\alpha}$  is the cross peak for which magnetization begins on C $\beta$  and ends on C $\alpha$ , and  $\tau$  is the length of the PDS mixing (see SI section 1.2 for further discussion). Figure 2 shows a <sup>13</sup>C PDS spectrum obtained at 60 kHz MAS with 1 s mixing, using the sample for which <sup>13</sup>C $\alpha$   $R_1$  will be measured. Traces are drawn through the most intense cross peaks, and the ratio of cross peak to diagonal peak is indicated. From these ratios, it is possible to put bounds on the spin-diffusion rates. It is also

possible to obtain some additional information when no cross peak is visible, if a diagonal peak is well-resolved and by assuming the cross-peak amplitude is less than twice the spectrum root mean squared amplitude (RMS), thus allowing upper bounds to be placed on the spin-diffusion rates. Several bounds obtained this way are given in Table 1.

**Table 1** Bounds on C $\alpha$ -C $\beta$  spin-diffusion rates

| Residue                | $(I_{\alpha\beta}/I_{\alpha\alpha})/\tau$<br>[s <sup>-1</sup> ] | $(I_{\beta\alpha}/I_{\beta\beta})/\tau$<br>[s <sup>-1</sup> ] | $(2 \cdot \text{RMS}/I_{\beta\beta})/\tau$<br>[s <sup>-1</sup> ] |
|------------------------|---|---|--|
| 260Thr                 | 0.27  | 0.36  | –  |
| 261Thr                 | 0.14  | 0.20  | –  |
| 241Leu                 | 0.05  | 0.07  | –  |
| Asn (226, 262, or 279) | 0.08  | 0.08  | –  |
| 239Val                 | –   | –   | <0.06  |
| 237Ala                 | –   | –   | <0.05  |
| 235Glu                 | –   | –   | <0.03  |
| 228Ala                 | –   | –   | <0.06  |

One first notes that the cross peaks identified (260T, 261T, and 241L) are the residues with the 1<sup>st</sup>, 7<sup>th</sup>, and 3<sup>rd</sup> smallest chemical-shift difference between C $\alpha$  and C $\beta$ , respectively. This seems unlikely to be coincidence, since a smaller chemical-shift difference will typically lead to more efficient spin diffusion (Ernst and Meier 1998). Peaks for which the spin-diffusion rate was bounded only by the diagonal peak intensity and the spectrum RMS show also low upper bounds to the <sup>13</sup>C–<sup>13</sup>C transfer rate. Aside from 260T, and 261T, the bounds on the rates here indicate that measurement of <sup>13</sup>C $\alpha$   $R_1$  rates should be dominated by relaxation processes and not by <sup>13</sup>C–<sup>13</sup>C transfer as can be seen by comparison to the  $R_1$  rate constants reported in the results section.

This raises the question why we are able to get relatively good results for measurement of <sup>13</sup>C $\alpha$   $R_1$  in uniformly <sup>13</sup>C labeled HET-s (218-289), whereas Asami et al. do not for uniformly <sup>13</sup>C labeled SH3 (Asami et al. 2015). A simple answer can be that we spin at 60 kHz MAS, as compared to Asami et al. who spin at 50 kHz. To test this, we compare median values of <sup>13</sup>C $\alpha$   $R_1$  for our sample at 50 kHz and at 60 kHz MAS, and find rates of 0.29 s<sup>-1</sup> and 0.21 s<sup>-1</sup>, a

nearly 40% increase in the measured rate at 50 kHz. Furthermore, when spinning to 65 kHz, the median rate is  $0.20 \text{ s}^{-1}$ ; this relatively small change between 60 and 65 kHz suggests that contributions from spin-diffusion are mostly quenched above 60 kHz. Plots of the residue specific rate constants are given in SI Figure 3.

Nonetheless, spinning to 60 kHz MAS may not always be sufficient to remove all  $^{13}\text{C}$ – $^{13}\text{C}$  transfer. Very weak  $\text{C}\alpha$ – $\text{C}'$  cross peaks appear in Figure 2, which is unexpected due to the large chemical-shift difference (Asami et al. observe similar results for SH3). For comparison, we measure a fully-protonated sample of uniformly  $^{13}\text{C}$  labeled MLF under the same conditions (60 kHz MAS), and find that there are no  $\text{C}\alpha$ – $\text{C}'$  cross peaks (see SI figure 4). The most likely explanation for appearance of  $\text{C}\alpha$ – $\text{C}'$  cross peaks in the sample of HET-s but not in MLF is that slower motion (ns– $\mu\text{s}$ ) in HET-s induces  $^{13}\text{C}$ – $^{13}\text{C}$  NOE (Kaiser 1963; Solomon 1955), whereas MLF has very little motion in this timescale to induce an NOE, although note that the protonation level is different in the MLF sample. This complicates the question as to whether  $^{13}\text{C}$ – $^{13}\text{C}$  transfer can be eliminated by faster spinning. NOE transfers due to microsecond (or slower) motions can in fact be reduced by faster spinning, however NOE transfers due to faster motion cannot be, and so the approach of preparing samples which do not have neighboring  $^{13}\text{C}$  may be the only viable approach if the NOE contribution is significant (Asami et al. 2015). However, NOE transfer does not appear to be a severe problem in our case, based on cross-peak analysis. Nonetheless, this study will have some systematic distortion of the  $^{13}\text{C}$   $R_1$  measurements due to potential additional  $^{13}\text{C}$ – $^{13}\text{C}$  relaxation pathways.

### 1.3 Transverse Relaxation ( $R_{1\rho}$ ) and the Violation of the Redfield Approximation

The ability to fit both  $R_1$  and  $R_{1\rho}$  data using the model-free approach allows one to utilize the extended model-free analysis to fit both slow and fast correlation times. Here, we investigate potential problems that may arise when utilizing the above listed equations for  $R_{1\rho}$  (Eqs. (5)-(7)). We begin by examining the behavior of  $R_{1\rho}$  as a function of the correlation time, because at some point Redfield theory will no longer be valid when the correlation time becomes too long. In order to investigate the range for which Eq. (5) is valid, we have used stochastic Liouville simulations (Abergel and Palmer 2003; Kubo 1963; Schneider and Freed 1989) of a dipole-coupled, two-spin system (without CSA) undergoing a two-site hop (Wittebort and Szabo 1978), where the opening angle between the two sites is  $5^\circ$ , and determined its  $R_{1\rho}$  for a wide range of correlation times, as shown in Figure 3. The simulation is performed in the laboratory frame of reference, which employs the full untruncated dipolar-coupling Hamiltonian,

and, therefore, gives numerically accurate results for the complete range of timescales. This calculation is compared to  $R_{1\rho}$  calculated based on Eq. (5), involving the Redfield approximation. In addition,  $R_{1\rho}$  is also calculated from a stochastic Liouville simulation in the rotating frame using the high-field truncated rotating-frame Hamiltonian. The calculation based on Eq. (5) is in very good agreement with the stochastic Liouville simulation in the laboratory frame for  $\tau_c < 320$  ns. However, for longer correlation times, the calculation deviates from the exact simulation, and at the maximum deviation it is 1.65 times larger than the correct  $R_{1\rho}$  value. To understand this failure, one must note that the Redfield approximation assumes that the magnetization does not evolve significantly within the correlation time of the motion (Redfield 1957). The calculated  $T_{1\rho}$  ( $T_{1\rho} = 1/R_{1\rho}$ ) is orders of magnitude longer than the correlation time,  $\tau_c$ , meaning that relaxation will not change the magnetization significantly within  $\tau_c$ . However, coherent behavior may also cause evolution of the magnetization. Since a perfect spin-lock cannot be obtained, some evolution of magnetization will occur due to the dipole coupling to the  $^1\text{H}$ . In SI Figure 5, we show how this evolution affects the amount of magnetization along the x-axis, and see that it causes an oscillation with a rate on the order of the rotor frequency. Therefore, although the magnetization refocuses periodically, the assumptions taken in Redfield theory can fail as the correlation time approaches the rotor frequency.

In contrast, the rotating-frame simulations that use the high-field approximation are in good agreement with the laboratory-frame simulation for  $\tau_c > 3.2$  ns. Therefore, we calculate  $R_{1\rho}$  based on Redfield theory using equations Eqs. (5) and (6) for  $\tau_c < 320$  ns, but use the stochastic Liouville simulations in the rotating frame for longer correlation times. In principle one could also use the laboratory-frame simulation for all timescales, but this is much more computationally expensive as discussed in SI section 1.7. Note that the motional models that we eventually use include multiple timescales. In this case, only one motion has  $\tau_c > 320$ , and so  $R_{1\rho}$  is determined via simulation for this motion, and  $R_{1\rho}$  contributions due to faster motions are determined using Eqs. (5) and (6), and all contributions to  $R_{1\rho}$  are simply added together.

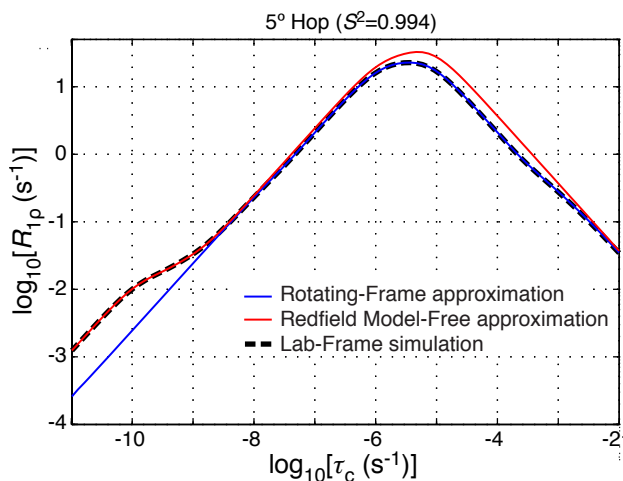


**Figure 3** Comparison of  $R_{1\rho}$  calculation methods. Here, we calculate  $R_{1\rho}$  for a  $^1\text{H}$ - $^{13}\text{C}$  spin system with  $\delta^{\text{IS}}/2\pi = 46.6$  kHz,  $\omega_r/2\pi = 60$  kHz, and  $\omega_1/2\pi = 35$  kHz, undergoing a hopping motion between two orientations, separated by  $5^\circ$ . The correlation time of this motion is swept. A simulation is performed in the lab-frame (black, dotted line), in the rotating frame (blue line), and a calculation is done using the model-free approach, with equation (5) (red line). The lab-frame simulation is numerically exact over the entire range of correlation times

Calculating  $R_{1\rho}$  based on Redfield theory using Eqs. (5) and (6) can still return qualitative results for slow motions, but particular care should be taken when fitting multiple timescales, as amplitude ( $S^2$ ) errors in the slow timescale can propagate to the fast timescale if the total amplitude of motion is characterized with  $S^2$  measurements. Further, when comparing results from different nuclei, one may find disagreement in the resulting timescales.

When measuring  $R_{1\rho}$ , one must also avoid the presence of coherent contributions to the decay of the spin-locked magnetization; in particular one must avoid the vicinity of the HORROR ( $\omega_1 = \omega_r/2$ ) (Nielsen et al. 1994) and rotary-resonance ( $\omega_1 = \omega_r$ ,  $\omega_1 = 2\omega_r$ ) (Oas et al. 1988) conditions. In principle, however,  $R_{1\rho}$  measured near the rotary-resonance condition may contain valuable information. This is because motions with long correlation times have little effect on the spectral-density function,  $J(\omega)$ , except when  $\omega$  is near to zero (see Eq. (1)). Therefore, in order to obtain information on slow motions, ideally one measures  $R_{1\rho}$  under conditions that sample  $J(\omega)$  near zero. From (5) and (6), we see that the condition  $\omega \approx 0$  is met when  $\omega_1 \approx \omega_r$  or  $\omega_1 \approx 2\omega_r$ , which is coincident with the rotary-resonance conditions. Therefore, one cannot sample  $J(0)$  exactly, but it is possible to work near this condition, as long as appropriate caution is taken and the coherent contributions to the decay can be neglected (see *below*).

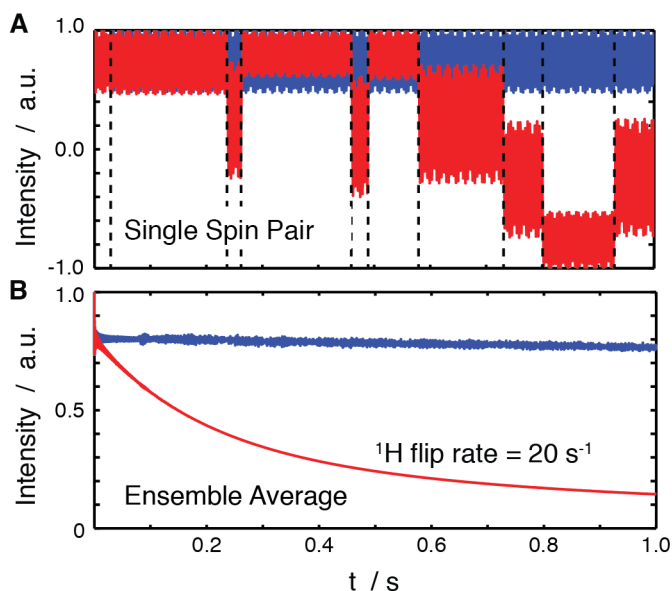


**Figure 4** Signal intensity as a function of time near the rotary-resonance condition. Here, a  $^1\text{H}$ - $^{13}\text{C}$  spin pair is simulated ( $\delta^{13}\text{C}/2\pi = 46.6$  kHz, no CSA), with  $\omega_r/2\pi = 60$  kHz, and  $\omega_1/2\pi = 48$  kHz. In (A), a single spin pair is considered (with Euler angles  $\alpha = 0^\circ$ ,  $\beta = 65^\circ$ ,  $\gamma = 0^\circ$ ), with (blue) and without flips (red) of the  $^1\text{H}$ . The flip positions are marked by dotted lines. In (B), an ensemble average is considered, without  $^1\text{H}$  flips (blue) and with  $^1\text{H}$  flips at a rate of  $20\text{ s}^{-1}$  (red)

In order to investigate measurement of  $R_{1\rho}$  near rotary resonance, we perform several simulations (see SI section 1.8 for details). The blue traces in Figure 4 show signal intensity for a single spin pair at a particular powder orientation and an ensemble average near the rotary resonance condition, in A and B respectively. The intensity corresponds to x-magnetization on the  $^{13}\text{C}$  spin. As one sees, oscillation due to the proximity to rotary resonance is periodically refocused for individual spin-pairs (Figure 4A, blue trace). For a powder average, some initial loss occurs since the spin pairs do not oscillate at the same frequency, but the total signal quickly equilibrates and only a very slow decay is observed at later times. However, if the  $^1\text{H}$  spin flips during the oscillation, then individual spin pairs do not refocus, as shown in Figure 4A, red trace. The net result is that the ensemble- and powder-averaged signal decays towards zero, as shown in Figure 4B, red trace.

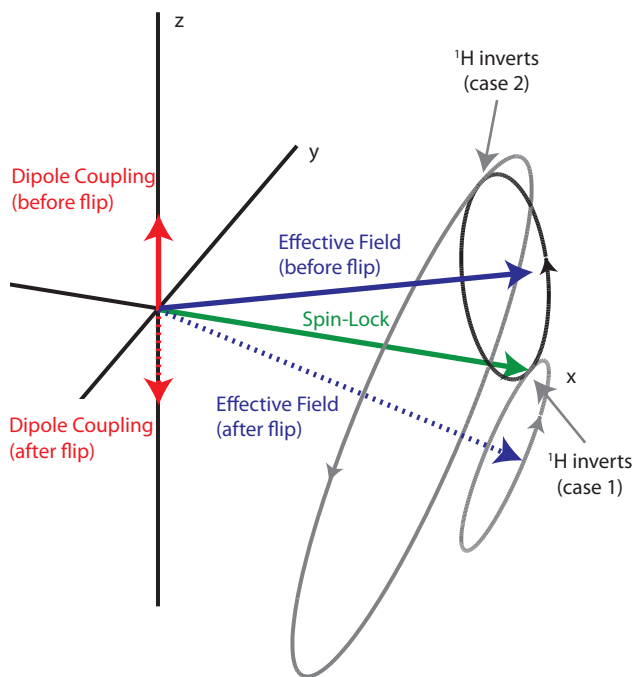


**Figure 5** Illustration of  $^{13}\text{C}$  or  $^{15}\text{N}$  magnetization trajectory in response to  $^1\text{H}$  spin flips. The field resulting from the dipole coupling (red), the field from the spin lock (green), and the resulting effective field (blue) are shown as solid lines. In black, the trajectory that the magnetization takes from the x-axis around the effective field is shown. After a  $^1\text{H}$  flip, the direction of the field from the dipole coupling and also the effective field are changed (dotted lines). The trajectory of magnetization is shown after the flip for the case that the magnetization is along the x-axis when the flip occurs (case 1), and for the case that the magnetization has rotated  $180^\circ$  around the effective field when the flip occurs (case 2). The first case results in no observable change of the projection of magnetization along the x-axis, but the second case reduces the projection.

To further illustrate this, we show a picture in Figure 5 for an example of signal decay, based on a static experiment. Then, there is no rotary resonance condition, but there is an effective field that depends on the spin-locking field and the dipole coupling- as well as the state of the  $^1\text{H}$  spin. Magnetization oscillates around the initial effective field (labeled as 'before flip'). Note that one measures the projection of magnetization onto the x-axis). Then, after some time the  $^1\text{H}$  flips, moving the effective field (labeled as 'after flip'). The effect this has on the magnetization depends when the  $^1\text{H}$  flips. Two extreme cases are shown. In the first case, magnetization has returned exactly to its starting location when the  $^1\text{H}$  flip occurs. This causes the magnetization to begin to oscillate from the x-axis to below the xy-plane, instead of above it, and so the projection of magnetization on the x-axis is unaffected. In the second case, the  $^1\text{H}$  flip occurs when the magnetization is  $180^\circ$  away from its starting position around the effective field. This results in the magnetization taking a much wider trajectory around the new effective field, and the projection of the magnetization on the x-axis is reduced. Repeated flips

like this will further deplete the magnetization on the x-axis. Of course, all cases in between these extremes will also occur, and will be averaged over the ensemble of spins. In the MAS case, the effective field is time dependent, although the analogy stands. Furthermore, the deviation of the trajectory of magnetization from the spin-locking field increases as rotary resonance is approached, therefore increasing the signal dephasing. This leads to faster  $R_{1\rho}$  dephasing due to  $^1\text{H}$  flips.

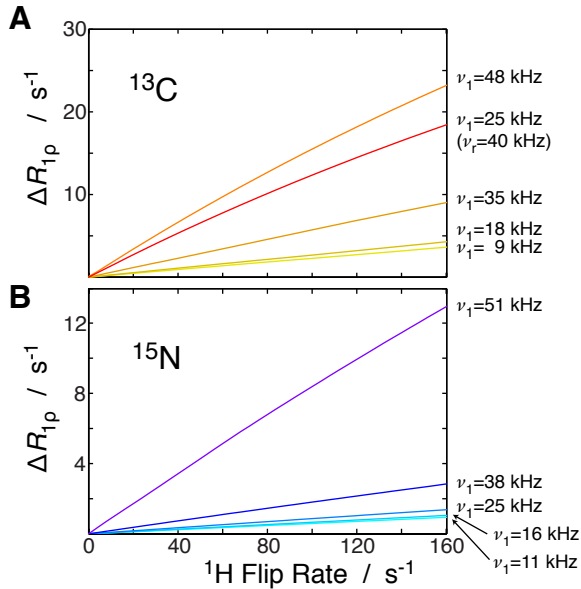


**Figure 6** Calculated  $\Delta R_{1\rho}$  rates as a function of the  $^1\text{H}$  flip rate. The  $\omega_1$  and  $\omega_r$  values chosen are those used in our experiments for  $^{13}\text{C}$  and  $^{15}\text{N}$ .  $\omega_r/2\pi = 60$  kHz for all curves except for the red line in (A), for which  $\omega_r/2\pi = 40$  kHz

The rate of magnetization decay due to  $^1\text{H}$  flips depends both on the proximity to the rotary-resonance condition and on the rate that  $^1\text{H}$  flips occur, which in turn depends on the MAS frequency,  $^1\text{H}$  density, and to some extent on the spin-lock strength applied to the heteronucleus (a major source of  $^1\text{H}$  flips is proton spin diffusion, see (Grommek et al. 2006; Takegoshi et al. 2003) for the dependency of spin diffusion on fields applied to other nuclei). However, the  $^1\text{H}$  flip rate can be measured (see section 2.2), and, therefore, this contribution can be calculated and compensated for in the data-evaluation process. Note that this is only possible because the contribution to  $R_{1\rho}$  from  $^1\text{H}$  inversion ( $\Delta R_{1\rho}^{(1\text{H} \text{ inver})}$ ) is approximately additive to other  $R_{1\rho}$  contributions, such that

$$R_{1\rho}^{(\text{exp})} \approx R_{1\rho}^{(\text{stoch})} + \Delta R_{1\rho}^{(1\text{H} \text{ inver})}. \quad (13)$$

We verify this via simulations that include both a stochastic motion and  $^1\text{H}$  inversions, and compare the resulting  $R_{1\rho}$  to simulations including only stochastic motion and only  $^1\text{H}$  inversion



(see SI Figure 6). Figure 6 shows this contribution to  $R_{1\rho}$  as a function of  $^1\text{H}$  flip rate, at the experimental conditions used in this study. Note the greater contributions seen for  $^1\text{H}\alpha$ - $^{13}\text{C}\alpha$  spin pairs compared to  $^1\text{H}$ - $^{15}\text{N}$  spin pairs. The site-specific corrections for our experimental data are given for  $^{15}\text{N}$  in Figure 7 and for  $^{13}\text{C}\alpha$  in SI Figure 7.

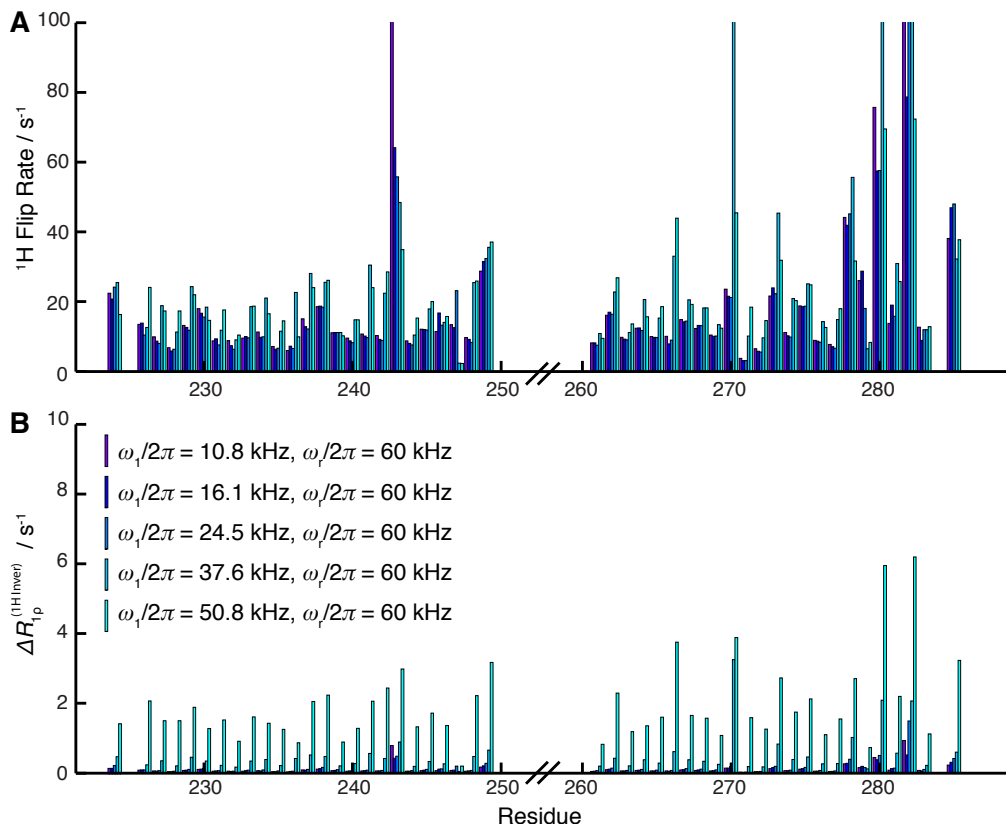


**Figure 7**  $^1\text{H}$  flip rate and  $R_{1\rho}$  correction. In (A), we show the measured  $^1\text{H}$  flip rate for each spin-lock and spinning frequency, matching the conditions used for measurement of  $^{15}\text{N}$   $R_{1\rho}$  relaxation. The rates shown in (A) are then used in (B) to calculate  $\Delta R_{1\rho}^{(^1\text{H}_{\text{inver}})}$ , the correction of the measured  $R_{1\rho}$  rate. The different experimental conditions are shown, with a different colored bar for each measurement condition, following the color code shown in (B)

To emphasize the importance of contributions to  $R_{1\rho}$  from  $^1\text{H}$  inversion, we illustrate how potential problems arise using a simple model simulation. For  $^{15}\text{N}$ , let us assume a motion with  $\tau_c = 3$  ns and an  $S^2 = 0.810$ , and for  $^{13}\text{C}\alpha$  we assume a motion with  $\tau_c = 3$  ns and  $S^2 = 0.880$ . We will also assume a  $^1\text{H}$  frequency of 850 MHz, for  $^{15}\text{N}$  we assume the anisotropy of the dipolar coupling to the  $^1\text{H}$  is  $\delta = 22.9$  kHz and the CSA is  $\Delta\sigma = 150$  ppm, and for  $^{13}\text{C}$  the coupling is  $\delta = 46.6$  kHz and the CSA is  $\Delta\sigma = 30$  ppm. If we use equation (7), we calculate for all values of  $\omega_1$  and  $\omega_r$  a  $^{15}\text{N}$   $R_{1\rho}^{(\text{stoch})}$  value of  $2.0$   $\text{s}^{-1}$  and a  $^{13}\text{C}\alpha$   $R_{1\rho}^{(\text{stoch})}$  of  $4.0$   $\text{s}^{-1}$ . However, the typical  $^1\text{H}$  inversion rates measured in this study fall in the range of  $10$ - $20$   $\text{s}^{-1}$ , although the full range is quite a bit broader (Figure 7 and SI Figure 7). Assuming, for both  $^{15}\text{N}$  and  $^{13}\text{C}\alpha$ , a

$^1\text{H}$  inversion rate of  $20\text{ s}^{-1}$ , different values of  $R_{1\rho}$  are obtained depending on the simulation conditions. The predicted rates ( $R_{1\rho}^{(\text{stoch})} + \Delta R_{1\rho}^{(1\text{H inversion})}$ ) as a function of the parameters are plotted as colored bars in Figure 8A for  $^{15}\text{N}$  and in Figure 8B for  $^{13}\text{Ca}$ . The rate constants obtained for  $^{15}\text{N}$   $R_{1\rho}$  are all greater than  $2.0\text{ s}^{-1}$ , and those obtained for  $^{13}\text{Ca}$   $R_{1\rho}$  are all greater than  $4.0\text{ s}^{-1}$ , with increasing deviation from  $R_{1\rho}^{(\text{stoch})}$  as the rotary-resonance condition is approached.

The problem becomes clear when one tries to fit these simulated  $R_{1\rho}$  rates to a motional model without considering the contribution by the  $^1\text{H}$  inversion. In this case, one finds that the  $R_{1\rho}$  can be reasonably well fit to a motional model with only a single motion, as shown in Figure 8A and B (black dots). For  $^{15}\text{N}$ , the fit to a single motion yields a correlation time of  $6.3\text{ }\mu\text{s}$  and  $S^2 = 0.998$ , and for  $^{13}\text{Ca}$  the correlation time is  $5.0\text{ }\mu\text{s}$  and  $S^2 = 0.997$ . Thus, the assumed motion with a  $3\text{ ns}$  correlation time and a relatively low order parameter has now been fitted to a single, microsecond motion with a much higher order parameter - a severe failure of the analysis. To avoid such a misinterpretation when using experimental data, it is important to either avoid experimental conditions that have a large contribution to the measured  $R_{1\rho}$  from  $^1\text{H}$  inversion ( $\Delta R_{1\rho}$ ), or measure the  $^1\text{H}$  inversion rate and correct for the effect. It is also worth noting that for  $^{13}\text{Ca}$ , where one of the simulation conditions involves a different MAS frequency, the fit to incorrect motion is much worse, so that acquiring  $R_{1\rho}$  at both different spin-locking frequencies and different MAS frequencies can help differentiate between true motion and magnetization decay induced by  $^1\text{H}$  inversion.

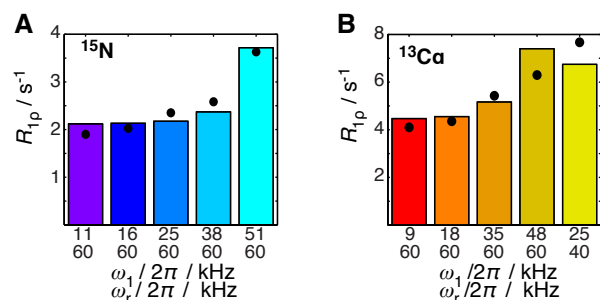


**Figure 8** Misinterpretation of  $R_{1\rho}$  caused by  $^1\text{H}$  inversion but interpreted as slow molecular motion. In (A), we take the  $^{15}\text{N}$  experimental settings for  $\omega_1$  and  $\omega_r$ , and use simulation to predict  $R_{1\rho}$  relaxation rates for a motion with  $\tau_c = 3\text{ ns}$  and  $S^2 = 0.810$  and for a  $^1\text{H}$  inversion rate of  $20\text{ s}^{-1}$  (colored bars). The simulated rates are then fitted to a model that only considers motion (no  $^1\text{H}$  inversion), using simulation of a slow motional, two-site hop with  $\tau_c = 6.3\text{ }\mu\text{s}$  and  $S^2 = 0.998$  (black dots). In (B), we do the same for our  $^{13}\text{Ca}$  experimental settings, this time for a motion with  $\tau_c = 3\text{ ns}$  and  $S^2 = 0.880$  and for a  $^1\text{H}$  inversion rate of  $20\text{ s}^{-1}$  (colored bars). We also fit to a simulation of a

slow motional, two-site hop model, in this case with  $\tau_c=5.0 \mu\text{s}$  and  $S^2=0.997$  (black dots). The fit is not as good, due to the usage of a different MAS frequency for the last data point

## 2 Experimental Methods

### 2.1 Sample Preparation

Measurement of dynamics data in the solid state requires minimization of undesired coherent interactions, so that measured relaxation rates on the X-nucleus can be attributed primarily to stochastic modulation of the X-CSA, and H–X dipole coupling of the bonded  $^1\text{H}$ . This is, in part, achieved by partial deuteration of the sample to be measured. An additional benefit to sample deuteration is that it improves resolution in the  $^1\text{H}$  dimension, making it possible improve sensitivity with  $^1\text{H}$  detection (Agarwal et al. 2014).

Therefore, samples were prepared to yield uniformly  $^{13}\text{C}$ ,  $^{15}\text{N}$  labeled HET-s, with partial deuteration. Samples for measurement of both  $^1\text{H}$ – $^{15}\text{N}$  and  $^1\text{H}\alpha$ – $^{13}\text{C}\alpha$  dynamics were prepared by recombinant expression of histidine-tagged HET-s (218-289) in *Escherichia coli* BL21 in M9 minimal medium (Balguerie et al. 2003). Uniformly labeled  $^2\text{H}$ ,  $^{13}\text{C}$  glucose was the sole carbon source, and  $^{15}\text{ND}_3\text{OD}$  was the sole nitrogen source. In the case of the sample for the study of  $^1\text{H}$ – $^{15}\text{N}$  dynamics, the growth solvent is pure  $\text{D}_2\text{O}$ , but fibrilization is performed in pure  $\text{H}_2\text{O}$  to yield a sample only protonated at exchangeable sites. For the sample for the study of  $^1\text{H}\alpha$ – $^{13}\text{C}\alpha$  dynamics, the growth solvent is 75%  $\text{D}_2\text{O}$  and 25%  $\text{H}_2\text{O}$ , and fibrilization is performed in  $\text{D}_2\text{O}$ . This growth medium yields 25% protonation at the  $\text{H}\alpha$  position, and limited protonation at other positions (Asami et al. 2010; Asami et al. 2012; Lundström et al. 2009). Fibrilization in  $\text{D}_2\text{O}$  eliminates protonation at exchangeable sites. Details of sample preparation, purification, and fibrilization are given in SI section 2.1.

### 2.2 Experiments

In order to precisely determine dynamics on multiple timescales, the direct order parameter  $S^2$ , three  $R_1$ , and five  $R_{1\rho}$  measurements (including  $^1\text{H}$  flip-rate measurements for  $R_{1\rho}$  correction) were acquired site specifically for the dynamics of both  $^1\text{H}\alpha$ – $^{13}\text{C}\alpha$  and  $^1\text{H}$ – $^{15}\text{N}$  vectors. The experiments are summarized in Table 2. All experiments were acquired using MAS at 60 kHz, unless otherwise noted, using a Bruker Advance III HD console (400, 500, and 850 MHz Larmor frequencies) and a 1.3 mm triple-resonance ( $^1\text{H}$ ,  $^{13}\text{C}$ ,  $^{15}\text{N}$ ) probe. Sample temperature was  $23.3\pm 0.3^\circ\text{C}$ , determined by referencing the supernatant water shift to DSS (Böckmann et al. 2009). Two-dimensional  $^1\text{H}$ – $^{15}\text{N}$  and  $^1\text{H}\alpha$ – $^{13}\text{C}\alpha$  correlation experiments were

used to obtain site resolution, where detection was performed on the  $^1\text{H}$  nucleus in order to maximize signal to noise. This required assigning the  $^1\text{H}$  resonances, which was done using the existing N, C $\alpha$ , C $\beta$ , and C' assignment (Siemer et al. 2006; Van Melckebeke et al. 2010); the details of the assignment will be provided elsewhere.

The pulse sequences used to measure dynamics data are shown in Figure 9. All sequences use an initial adiabatic cross-polarization step (Hediger et al. 1995) to the heteronucleus of interest to boost the initial polarization ( $^{15}\text{N}$  or  $^{13}\text{C}\alpha$ ) and water suppression using a modified MISSISSIPPI sequence (Zhou and Rienstra 2008) ( $\pi/2$  pulses are inserted after each saturation period). Magnetization is then transferred back to  $^1\text{H}$  from the heteronucleus, and signal is detected on  $^1\text{H}$ . Detailed experimental parameters are provided in SI section 2.2.

**Table 2** Experiments and Parameters

| Nucl.           | Type                                      | # Exper.<br>(total time)          | Critical Parameters          |                              |                              |
|-----------------|---|-----------------------------------|------------------------------|------------------------------|------------------------------|
| $^{13}\text{C}$ | REDOR                                     | 1 (215 hrs)                       | $\omega_r/2\pi = 60$ kHz     | $\omega_{0H}/2\pi = 850$ MHz | $\omega_{1H}/2\pi = 150$ kHz |
| $^{13}\text{C}$ | $R_{1\rho}$<br>(+ $^1\text{H}$ flip rate) | 5 (+5)<br>(331 hrs,<br>+ 251 hrs) | $\omega_r/2\pi = 60$ kHz     | $\omega_{0H}/2\pi = 500$ MHz | $\omega_1/2\pi = 9.3$ kHz    |
|                 |   |                                   | $\omega_r/2\pi = 60$ kHz     | $\omega_{0H}/2\pi = 500$ MHz | $\omega_1/2\pi = 17.5$ kHz   |
|                 |   |                                   | $\omega_r/2\pi = 60$ kHz     | $\omega_{0H}/2\pi = 850$ MHz | $\omega_1/2\pi = 35.0$ kHz   |
|                 |   |                                   | $\omega_r/2\pi = 60$ kHz     | $\omega_{0H}/2\pi = 850$ MHz | $\omega_1/2\pi = 47.7$ kHz   |
| $^{13}\text{C}$ | $R_1$                                     | 3 (396 hrs)                       | $\omega_{0H}/2\pi = 400$ MHz | $\omega_{0H}/2\pi = 500$ MHz | $\omega_{0H}/2\pi = 850$ MHz |
| $^{15}\text{N}$ | REDOR                                     | 1 (123 hrs)                       | $\omega_r/2\pi = 60$ kHz     | $\omega_{0H}/2\pi = 850$ MHz | $\omega_{1H}/2\pi = 150$ kHz |
| $^{15}\text{N}$ | $R_{1\rho}$<br>(+ $^1\text{H}$ flip rate) | 5 (+5)<br>(358 hrs, +<br>156 hrs) | $\omega_r/2\pi = 60$ kHz     | $\omega_{0H}/2\pi = 850$ MHz | $\omega_1/2\pi = 10.8$ kHz   |
|                 |   |                                   | $\omega_r/2\pi = 60$ kHz     | $\omega_{0H}/2\pi = 850$ MHz | $\omega_1/2\pi = 16.1$ kHz   |
|                 |   |                                   | $\omega_r/2\pi = 60$ kHz     | $\omega_{0H}/2\pi = 850$ MHz | $\omega_1/2\pi = 24.5$ kHz   |
|                 |   |                                   | $\omega_r/2\pi = 60$ kHz     | $\omega_{0H}/2\pi = 500$ MHz | $\omega_1/2\pi = 37.6$ kHz   |
| $^{15}\text{N}$ | $R_1$                                     | 3 (519 hrs)                       | $\omega_{0H}/2\pi = 400$ MHz | $\omega_{0H}/2\pi = 500$ MHz | $\omega_{0H}/2\pi = 850$ MHz |

In both  $R_1$  and  $R_{1\rho}$  sequences, magnetization is allowed to decay, either as longitudinal magnetization for  $R_1$  measurements (Figure 9A), or as spin-locked magnetization for  $R_{1\rho}$

(Figure 9B). The sequence shown in Figure 9C measures the  $^1\text{H}$  flip rate required for the correction of the  $R_{1\rho}$  data. Since initially the net magnetization is roughly equal at all sites, it is necessary to first perform the indirect dimension so that polarization is unequal for the different  $^1\text{H}$ , allowing polarization transfer between them. This also means that signal gains due to spin-diffusion from different sites appear as cross-peaks, and so do not distort the measurement of  $^1\text{H}$  flip rate on the peaks of interest (assuming separation between the cross peaks and the peaks of interest). Note that an RF-field is applied to the heteronucleus during measurement of the  $^1\text{H}$  flip rate. This field needs to match that used during the corresponding  $R_{1\rho}$  measurement, because couplings to  $^{13}\text{C}$  or  $^{15}\text{N}$  spins assist  $^1\text{H}$  spin-diffusion, and so fields applied to those spins may change the spin-diffusion rates (Grommek et al. 2006; Takegoshi et al. 2001). Because a major source of  $^1\text{H}$  flips is spin-diffusion, it is possible to observe bi-exponential (or multi-exponential) behavior when measuring the  $^1\text{H}$  flip rate, due to build up of magnetization on neighboring  $^1\text{H}$ 's. In this case, it is not yet clear whether one can correct the  $R_{1\rho}$  to account for  $^1\text{H}$  spin-diffusion. However, if spin-diffusion does not result in significant buildup on neighboring  $^1\text{H}$ 's (due to sufficiently fast  $R_1$  or diffusion to more distant protons, for example), then nearly monoexponential behavior is seen, as was observed in our experiments (see SI Figure 17 for plots of the  $^1\text{H}$  behavior), and we can perform the  $R_{1\rho}$  correction. One must also be careful that new cross-peaks do not overlap peaks of interest, and therefore distort the extracted  $^1\text{H}$  flip rate- although we also did not encounter this problem.

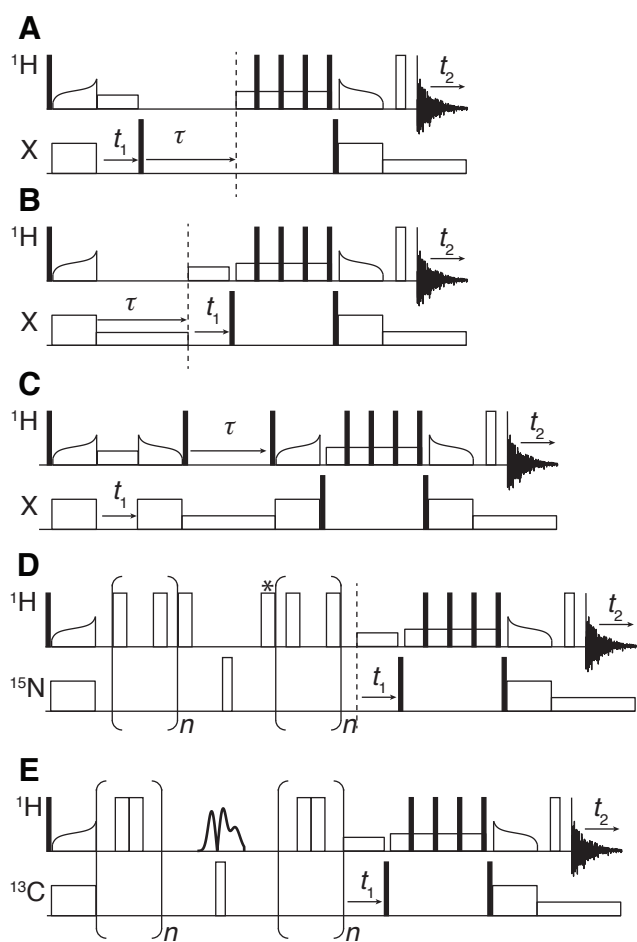


**Figure 9** Pulse sequences for 2D experiments to measure dynamics data. A) and B) are  $R_1$  and  $R_{1\rho}$  measurement sequences, respectively, where  $\tau$  is incremented to obtain relaxation curves. C) measures the  $^1\text{H}$  flip rate, under the same conditions as the  $R_{1\rho}$  measurements. D) shows the shifted-REDOR sequence, which is used to measure  $^1\text{H}$ - $^{15}\text{N}$  residual dipole couplings. The \* indicates the pulse that could be replaced with a selective pulse for selective REDOR. E) shows the REDOR sequence that is used to measure  $^1\text{H}\alpha$ - $^{13}\text{C}\alpha$  couplings by frequency-selecting the  $^1\text{H}\alpha$  resonances. For both D) and E), XY-16 phase cycling (Gullion et al. 1990) is used to compensate pulse error (with mirroring of phases around the center of the REDOR period), and  $n$  is incremented to obtain REDOR curves.  $S_0$  reference curves are obtained by omitting all  $^1\text{H}$   $\pi$ -pulses during the dephasing period

The REDOR sequence is used to measure the  $^1\text{H}$ - $^{15}\text{N}$  and  $^1\text{H}\alpha$ - $^{13}\text{C}\alpha$  dipolar couplings (Gullion and Schaefer 1989b) because of its robustness against RF inhomogeneity and incorrect settings of the RF field strength (Schanda et al. 2011). The scaling factor of the standard REDOR sequence (Jaroniec et al. 2000) is too large for the measurement of one-bond dipole couplings at fast MAS frequencies. This problem can be overcome by shifted-time REDOR, where the pulses in the center of the rotor period are shifted in order to reduce the

effective recoupling strength (mirror-symmetric REDOR, (Gullion and Schaefer 1989a)), as shown in Figure 9D. We use this sequence for obtaining  $^1\text{H}$ - $^{15}\text{N}$  order parameters.

Measuring  $^1\text{H}\alpha$ - $^{13}\text{C}\alpha$  order parameters is more challenging, because our isotope-labeling scheme leads to some residues protonated at the  $^1\text{H}\alpha$  position as well as at the  $^1\text{H}\beta$  position. Frequency-selective REDOR (Jaroniec et al. 2001) can be used to only recouple H-C couplings for which the H resonance is within a given frequency range, making it possible to exclude most  $\text{H}\beta$ - $\text{C}\alpha$  couplings. However, frequency-selective REDOR is not compatible with mirror-symmetric shifted REDOR shown in Figure 9D. The reason for this is that frequency-selective REDOR uses a selective pulse on the  $^1\text{H}$  channel in the center of the REDOR period, which replaces the first pulse after the center of the sequence (marked with a \* in Figure 9). Then, the  $^1\text{H}$ -X dipole couplings of  $^1\text{H}$ 's that are inverted by the selective pulse are refocused by the frequency-selective REDOR sequence, whereas dipole couplings of  $^1\text{H}$ 's that are not inverted by the selective pulse are not refocused, because the second half of the REDOR period reverses the recoupling achieved in the first half of the REDOR period. When one uses the mirror-symmetric shifted REDOR shown in Figure 9D, however, one finds that if the first pulse after the center of the REDOR period (marked with a \*) is removed, recoupling is still achieved- although the rate of recoupling is not the same as if the pulse is included. Therefore, even if a selective pulse is used, the dipole couplings to  $^1\text{H}$ 's that are not inverted with a selective pulse are also recoupled but with a smaller scaling factor. To resolve this, we have modified the REDOR sequence as shown in Figure 9E. In fact, the sequence used here is very similar to the mirror asymmetric sequences presented in (Gullion and Schaefer 1989a), because the first and second half of the sequence are identical without mirroring. Therefore, if the  $^1\text{H}$  is not inverted in the center of the sequence, the recoupling achieved in the first half of the sequence is reversed in the second half, making it possible to use selective REDOR. One does need to be careful, however, since not all  $\text{H}\beta$  chemical shifts are well separated from the  $\text{H}\alpha$  chemical shifts.

Note that although the  $\pi$ -pulses in our sequence are immediately next to each other, we still have recoupling. When using fast MAS, in our case 60 kHz, strong  $\pi$ -pulses still take up a significant part of the rotor period (e.g. two 150 kHz  $\pi$ -pulses take 40% of the rotor period). Therefore, two  $\pi$ -pulses placed immediately next to each other in the center of the rotor period significantly reduce the effective dipole coupling during that period, and so the dipole coupling is no longer completely averaged by MAS (see SI Figure 8 for calculation of a time-trace). For the selective pulse, we use a Q3 pulse (Emsley and Bodenhausen 1992), with bandwidth set

to cover the  $^1\text{H}\alpha$  chemical shift range (at a  $^1\text{H}$  frequency of 850 MHz, this resulted in a 1376  $\mu\text{s}$  pulse, 3.2 kHz bandwidth- defined by the width where at least 50% inversion occurs). We utilize XY-16 phase cycling (Gullion et al. 1990) as in the shifted REDOR sequence. We check that the measured  $^1\text{H}\alpha$ - $^{13}\text{C}\alpha$  dipole couplings are not strongly scaled by our sequence, a serious problem for dynamics analysis resulting from radio-frequency (RF) inhomogeneities, which has been investigated in detail for  $^1\text{H}$ - $^{15}\text{N}$  dipole couplings (Haller and Schanda 2013). We check for scaling by refitting our REDOR data set with a uniform scaling factor multiplied by the measured dipole couplings, and optimizing that scaling factor to best-fit the data. Ultimately, we scaled our dipole couplings up by a factor of 1.012, a relatively small amount.

### 3 Data Analysis

Each dynamic parameter measurement is acquired as a series of 2D experiments, where the value of either  $\tau$ , or  $n$  for REDOR experiments, is incremented (see Figure 9). We then extract the amplitude for each cross peak in all spectra. This yields time-dependent intensities for each resonance (selected measurements given in SI Figures 17-21), which are then fitted to determine relaxation-rate constants and scaled dipolar couplings, and finally the acquired dipolar couplings and relaxation rates are fitted to a dynamic model. The details of each step are presented in this chapter.

#### 3.1 Spectrum Fitting

A significant amount of overlap of resonances in both 2D  $^1\text{H}$ - $^{15}\text{N}$  and  $^1\text{H}$ - $^{13}\text{C}$  spectra make extraction of accurate amplitudes for each residue difficult using either peak maxima or peak integration (see SI Figure 9). Therefore, we have developed an automated spectrum-fitting routine, using MATLAB (The MathWorks 2013). For our purposes, it is critical to have precise fitting of the spectra; in particular, peak shapes must be as accurate as possible. Incorrect shapes result either in fitting of incorrect amplitudes of neighboring peaks due to the overlap, or one must add extra peaks to fit out these extra errors leading to over-fitting, and, therefore, introducing additional noise into the extracted data.

In order to have optimal results, we fit the experimental spectrum using peak shapes that are calculated based on acquisition and processing parameters; in particular acquisition time, apodization function, and zero-filling are used to generate accurate peak shapes. The type of signal decay is user specified in each dimension (Gaussian, exponential, or some



mixture), and we vary the type of decay to further improve fitting. A more complete description of this program will be presented in a separate publication.

In order to extract intensities from 2D spectra, we begin by generating a reference fit for each of the two data series: one for H $\alpha$ –C $\alpha$  2D spectra and one for H–N 2D spectra. The resulting fits are shown in SI Figure 9 where the experimental and fitted spectra are shown along with several traces to show the fit quality. The program determines number of peaks, peak positions, line widths, and intensities for the reference fits. Then for each data series, the number of peaks and the peak positions are fixed for all consecutive fits. However, the line widths are re-optimized, to account for different magnetic fields, and other smaller variations in experimental conditions. Once the line widths are re-optimized for a data series, then each spectrum in the series is fitted by only allowing the intensities to vary. By fixing as many parameters as possible, the influence that overlap of neighboring peaks has on the measured intensities is minimized. Note that this method makes the quality of the initial fits critical, and in general makes spectrum phasing and referencing very important. Examples of the resulting time traces are given in SI Figures 17-21.

### 3.2 Parameter and Error Determination

After intensities are extracted from the 2D spectra, it is necessary to determine relaxation rates or partially-averaged dipolar couplings from the data. For all relaxation rates except  $^{15}\text{N}$   $R_{1\rho}$ , the intensity data is fitted to a mono-exponential decay

$$I_k = A \exp(-R\tau_k), \quad (14)$$

where  $R = R_1$  or  $R_{1\rho}$ , and  $A$  accounts for the differences in intensities for different resonances. We also use this formula to extract the rate of  $^1\text{H}$  inversion from experimental data, and furthermore for extracting  $R_{1\rho}$  values from simulations. When fitting  $^{15}\text{N}$   $R_{1\rho}$ , we have to fit the data to a bi-exponential function:

$$I_k = \frac{A}{2} (\exp(-R_a\tau_k) + \exp(-R_b\tau_k)) \quad (15)$$

This is a result of significant contributions from CSA/dipole cross-correlated cross relaxation to the spin-locked two-spin term ( $2I_xS_z$ ) leading to a bi-exponential decay of the magnetization. Another way of looking at this is that the two lines of the  $^{15}\text{N}$  multiplett ( $I_xS_\alpha$  and  $I_xS_\beta$ ) decay with two different relaxation-rate constants. However,  $^1\text{H}$  inversion causes these two rates to partially average, and in the limit of fast flipping,  $R_a = R_b$ . Therefore, the ratio of  $R_a$  to  $R_b$  changes for different residues, but the average of these two rates is independent of the flip rate

and we report  $R_{1\rho} = (R_a + R_b)/2$ . Note that this is the rate predicted by Redfield theory (see Eq. (7), and if we compare to a stochastic Liouville simulation, we may also take the average of the bi-exponential fit of the simulated curve.

REDOR data consists of two data sets:  $S$  curves, which give dephasing due to coupling between the  $^1\text{H}$  and the heteronucleus, and  $S_0$  curves, which have the  $^1\text{H}$   $\pi$  pulses omitted (note that  $S$  and  $S_0$  here should not be confused with the order parameter,  $S^2$ ). The length of our dephasing period is relatively short (600  $\mu\text{s}$  for  $^1\text{H}\alpha$ - $^{13}\text{C}\alpha$ , 1.33 ms for  $^{15}\text{N}$ ), so that the decay of the  $S_0$  curve is linear in this range. Therefore, we only acquire a few  $S_0$  spectra, using linear regression to fit the  $S_0$  to a straight line so that for a particular residue,

$$S_{0,k} = m\tau_k + b. \quad (16)$$

Then the REDOR curve is given by

$$I_k = \frac{S_{0,k} - S_k}{S_{0,k}}, \quad (17)$$

and the intensities  $I_k$  are fit to amplitudes determined by simulating the appropriate pulse sequence in SIMPSON (Bak et al. 2000) with a two-spin system, where the order parameter ( $S^2 = (\delta^{\text{IS}}_{\text{obs}}/\delta^{\text{IS}}_{\text{rigid}})^2$ ) is varied to achieve a fit. For  $^1\text{H}\alpha$ - $^{13}\text{C}\alpha$  REDOR curves, the simulated amplitudes are also fitted with an additional scaling factor ( $I_k^{\text{fit}} = A I_k^{\text{sim}}$ ). Imperfect inversion of the  $^1\text{H}\alpha$  by the selective pulse (Figure 9E) decreases the dephasing amplitude, although otherwise does not significantly impact the shape of the dephasing curve. The additional scaling factor accounts for this.

For all parameters, it is also necessary to know the error of the measurement. We obtain a standard deviation by bootstrapping our data (Efron and Tibshirani 1993): first, we obtain a best fit of the data to the model, and then assume that

$$I_{\text{exp},k} = I_{\text{model},k} + \varepsilon_k, \quad (18)$$

where  $\varepsilon_k$  is the error at data point  $k$ . Then, a bootstrapped data set is generated using

$$I_{\text{bootstrap},k} = I_{\text{model},k} + \varepsilon_m, \quad (19)$$

where  $\varepsilon_m$  is a randomly selected error (with replacement) from the  $\varepsilon_k$  of the original fit. The bootstrapped intensities are then refit, to obtain a new value of the parameter of interest ( $R_1$ ,  $R_{1\rho}$ ,  $S^2$ ). The bootstrapping process is repeated 100 times, and the standard deviation of the fitted parameters obtained from the bootstrapped data is taken to obtain the measurement standard deviation ( $\sigma$ ). The advantage of using a bootstrap to determine error is that it inherently includes all sources of error occurring within a given data set. This then includes

spectral noise, as well as other experimental variations- such as instrumental instabilities and temperature variation within a data set. It will not include variations that occur between data sets, however, and so we must take care to control sample quality, temperature, etc.

### 3.3 Fitting to a Dynamic Model

For each  $^1\text{H}\alpha\text{-}^{13}\text{C}\alpha$  and  $^1\text{H}\text{-}^{15}\text{N}$  spin pair, we have several experimental parameters ( $R_1$ ,  $R_{1\rho}$ , and  $S^2$ ), which must be fitted to a dynamic model that is characterized by multiple amplitudes ( $S_i^2$ ) and timescales ( $\tau_i$ ) of motion. Then, we can compare the experimental parameters to those calculated from the dynamic model using a  $\chi^2$ -statistic as follows:

$$\chi_v^2 = \frac{(S_{\text{exp}} - S_{\text{calc}})^2}{(\sigma(S))^2} + \sum_{k=1}^{N_{R_1}} \frac{(R_{1,k}^{\text{exp}} - R_{1,k}^{\text{calc}})^2}{(\sigma(R_{1,k}))^2} + \sum_{k=1}^{N_{R_{1\rho}}} \frac{(R_{1\rho,k}^{\text{exp}} - R_{1\rho,k}^{\text{calc}})^2}{(\sigma(R_{1\rho,k}))^2}. \quad (20)$$

Equation (20) contains the calculated values for all experiments, the experimental values, and the experimental standard deviation.  $v$  is the degrees of freedom of the  $\chi^2$  distribution, given by the number of experimental parameters ( $N_{R_1} + N_{R_{1\rho}} + 1$ ) minus the number of fit parameters. Minimizing the value of  $\chi^2$  by varying the dynamic model parameters then returns a fit to the dynamic model that favors the more precisely measured parameters. We report the reduced- $\chi^2$  in later figures, which is given by  $\chi^2/v$ . We additionally estimate the 68% confidence interval for each parameter, by finding the range on that parameter for which  $\chi^2 < \chi^2_{\text{min}} + 1$ , where  $\chi^2_{\text{min}}$  is minimized value of  $\chi^2$  (Clifford 1973). Details of the error analysis and the  $\chi^2$  minimization are given in section 3.2 of the SI.

When fitting experimental parameters to dynamic models, we will use either two or three timescales of motion. If a motion has a correlation time longer than 320 ns,  $R_{1\rho}$  will be calculated using stochastic-Liouville simulations in the rotating frame, otherwise it will be calculated using Redfield theory (Eq. (7)).  $R_1$  is always calculated using Redfield theory (Eq. (4)), because slow motions with correlation times longer than 320 ns will have a negligible contribution to  $R_1$ . We assume for all calculations or simulations a  $^1\text{H}\alpha\text{-}^{13}\text{C}\alpha$  bond distance of 1.09 Å, a  $^1\text{H}\text{-}^{15}\text{N}$  bond distance of 1.02 Å, a  $^{13}\text{C}\alpha$  CSA of 20 ppm (although this is almost negligible), and a  $^{15}\text{N}$  CSA of  $\Delta\sigma=170$  ppm. The  $^{13}\text{C}\alpha$  CSA is assumed to be axially symmetric and collinear with the  $^1\text{H}\alpha\text{-}^{13}\text{C}\alpha$  dipole coupling. The  $^{15}\text{N}$  CSA is assumed to have an asymmetry of  $\eta = 0.4$  (Wylie et al. 2006), and Euler angles of ( $\alpha=30^\circ, \beta=25^\circ, \gamma=0^\circ$ ) (Hou et al. 2010).

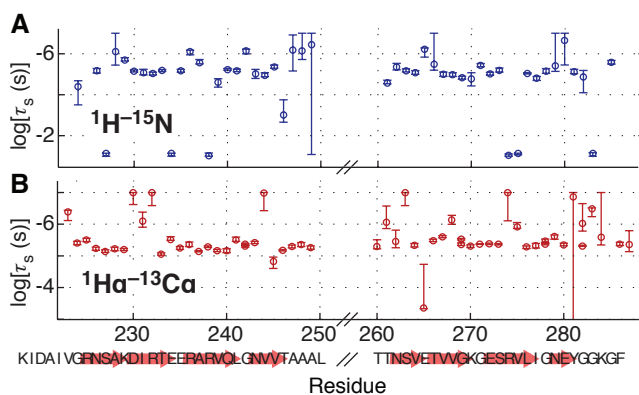


**Figure 10** Slow timescales ( $\tau_s$ ) determined using a 4-parameter fit ( $S_f^2$ ,  $\tau_f$ ,  $S_s^2$ ,  $\tau_s$ ) for both  $^1\text{H}\alpha$ - $^{13}\text{C}\alpha$  and  $^1\text{H}$ - $^{15}\text{N}$  dynamics, shown in (A) and (B), respectively. We only show the slow timescale, to illustrate that the distribution is rather narrow, in particular for  $^1\text{H}\alpha$ - $^{13}\text{C}\alpha$ , and similar for both spins, an argument that this is likely to be a single, concerted motion

#### 4 Results and Discussion

We begin investigating the HET-s dynamics by fitting both data sets ( $^{15}\text{N}$  and  $^{13}\text{C}\alpha$ ) independently to dynamic models. Previously, it has been shown that when incorporating both  $R_1$  and  $R_{1\rho}$  at multiple external fields and multiple spin-locking strengths (and spin-locking frequency offsets), that a three-timescale fit provides a statistically significant, better fit of the relaxation data (Zinkevich et al. 2013). Therefore, we will investigate both two- and three-timescale fits for our results. We begin by fitting the  $^{15}\text{N}$  and  $^{13}\text{C}\alpha$  data sets to models that incorporate two timescales of motion, and, therefore, four fit parameters ( $S_f^2$ ,  $\tau_f$ ,  $S_s^2$ ,  $\tau_s$ ). Figure 10 shows the site-specific slow correlation times resulting from this fit (note that for some glycine residues, the two  $\text{H}\alpha$  yield different chemical shifts and can be analyzed separately, and so here and throughout the paper two values appear for these residues). The results indicate that there is slow motion detected throughout the HET-s (218-289) fibril. Furthermore, timescales of  $\sim 10 \mu\text{s}$  indicate concerted motions of at least several atoms or more (Henzler-Wildman and Kern 2007). In fact, the narrow distribution of timescales for  $^1\text{H}\alpha$ - $^{13}\text{C}\alpha$  and  $^1\text{H}$ - $^{15}\text{N}$  suggests that the entire molecule may see a single, slow motion- similar to results of a recent study on crystalline Ubiquitin (Ma et al. 2015). Since a concerted motion should have approximately the same correlation time for all residues, we will require that all residues are fitted to the same slow correlation time,  $\tau_s$ . This has the added benefit that we reduce the number of parameters required to fit our data.

To find  $\tau_s$ , its value is varied and the complete experimental data set is refit at each value, by optimizing the remaining parameters, which are  $S_s^2$ ,  $\tau_f$ , and  $S_f^2$  if a two-timescale

model is used, and  $S_s^2$ ,  $\tau_i$ ,  $S_i^2$ ,  $\tau_f$ , and  $S_f^2$  if a three-timescale model is used ( $s$ ,  $i$ , and  $f$  indicate slow, intermediate and fast). Then the reduced- $\chi^2$  (sum of  $\chi^2$  for all residues, divided by total number of measured parameters minus number of fit parameters) is calculated at each value of  $\tau_s$  to determine the best value for each model. This is done both for  $^{15}\text{N}$  and  $^{13}\text{Ca}$  data sets, and for both two-timescale and three-timescale models, and plotted against the slow correlation time,  $\tau_s$ , shown in Figure 11A and B, respectively. As one sees, the best reduced- $\chi^2$  value for both nuclei is found when using the three-timescale model. For the two-timescale model, the best fit value of  $\tau_s$  was found to be 6.2  $\mu\text{s}$  and 4.1  $\mu\text{s}$  for  $^1\text{H}$ - $^{15}\text{N}$  and  $^1\text{H}\alpha$ - $^{13}\text{Ca}$  slow motion, respectively. For the three timescale model,  $\tau_s$  was found to be 14.7  $\mu\text{s}$  and 8.7  $\mu\text{s}$ , for  $^1\text{H}$ - $^{15}\text{N}$  and  $^1\text{H}\alpha$ - $^{13}\text{Ca}$  motion, respectively.

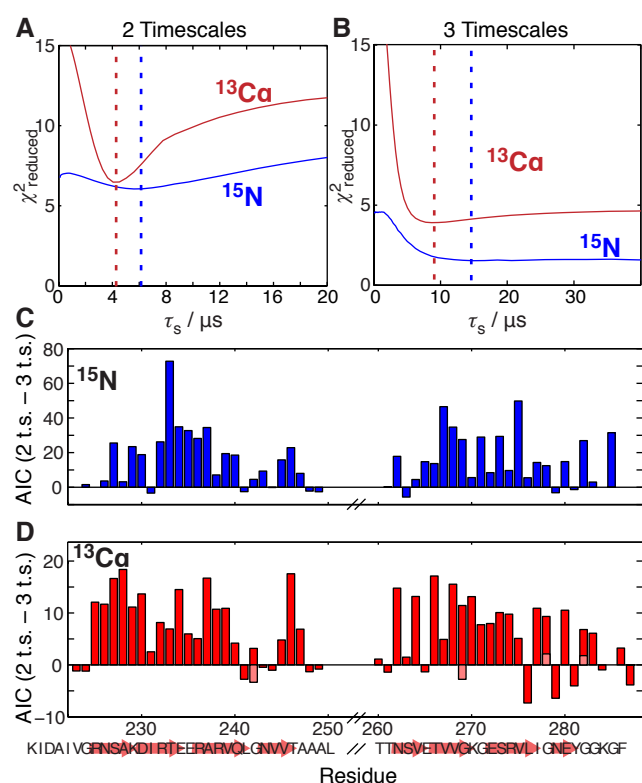


**Figure 11** Statistical comparison of two- and three-timescale models for  $^{15}\text{N}$  and  $^{13}\text{Ca}$ . (A) shows the reduced- $\chi^2$  (calculated over all residues) for the two-timescale model for both  $^{15}\text{N}$  and  $^{13}\text{Ca}$  data as a function of the slow correlation time,  $\tau_s$ , which is set to be the same for all residues. (B) shows the reduced- $\chi^2$  for the three-timescale model for both  $^{15}\text{N}$  and  $^{13}\text{Ca}$  data as a function of  $\tau_s$ . (C) is the residue specific difference of the AIC parameter for the two- and three-timescale models for  $^{15}\text{N}$ , and (D) is the difference for  $^{13}\text{Ca}$ , where positive values indicate that the three-timescale model better fits the data

To further investigate the choice of model, we evaluate the residue-specific fit quality with the Akaike Information Criterion (AIC) (Abdullah et al. 2013; Akaike 1974). This allows comparison of two models to determine which better fits the data, while also accounting for the number of fitting parameters being used.

$$AIC = N \ln(\chi^2 / N) + 2K. \quad (21)$$

Here,  $N$  is the number of experimental parameters (3  $R_1$ , 5  $R_{1\rho}$ , and 1  $S^2$  yields  $N=9$ ),  $\chi^2$  is as given in (20), and  $K$  is the number of fitting parameters (3 or 5 depending on whether we use the two- or three-timescale model, noting that we do not count the slow correlation time,  $\tau_s$ , since it is fitted against the full data set and does not significantly contribute to the degrees of freedom of an individual residue). The model for which the AIC parameter is smaller is then considered to be the better model, while taken into account both fit quality and number of fit parameters. The results for  $^{15}\text{N}$  and  $^{13}\text{C}\alpha$  analysis are shown in in Figure 11C and D, respectively, where the difference in the AIC for the two-timescale model and the three-timescale model is plotted against the residue number (positive values indicate that the three-timescale model is better).

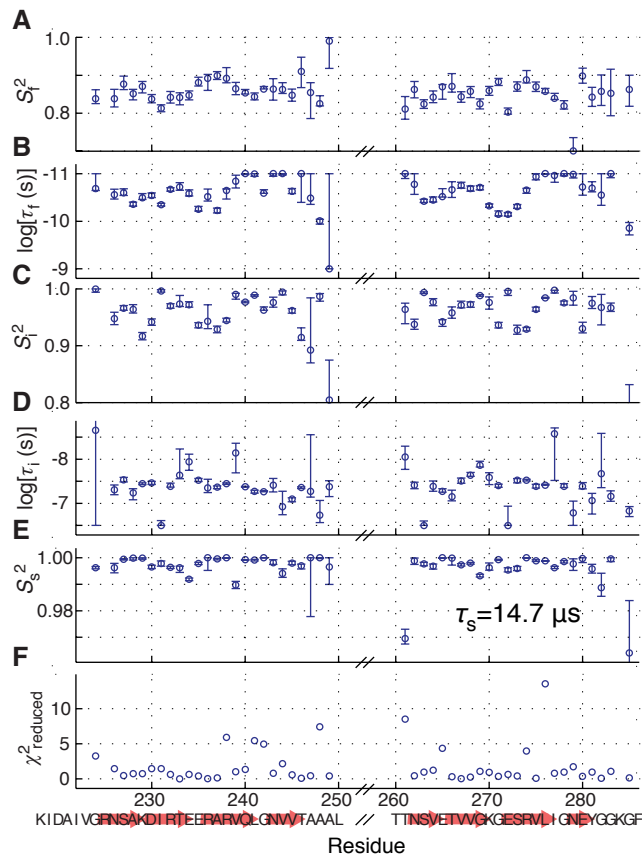


**Figure 12** Fit parameters for  $^1\text{H}$ - $^{15}\text{N}$  dynamics using a three-timescale model. (A) gives the residue specific fast motional amplitude ( $S_f^2$ ). (B) gives the fast motional timescale ( $\tau_f$ ), plotted logarithmically. (C) and (D) give the

intermediate motional timescale ( $\tau_i$ ), and amplitude ( $S_i^2$ ). (E) gives the slow motional amplitude ( $S_s^2$ ), using a correlation time of  $\tau_s = 14.7 \mu\text{s}$ . (F) gives the reduced- $\chi^2$  of the fit. (A-E) show error bars, which approximate a 68% confidence interval for the parameter

The three-timescale model fits the majority of residues better for both data sets. In Figure 12 the fit is given for  $^1\text{H}$ - $^{15}\text{N}$  motion and in Figure 13 the fit is given for  $^1\text{H}\alpha$ - $^{13}\text{C}\alpha$ , with comparison of calculated and experimental data in Figure 14 and Figure 15. We find that nearly all of the residues for which the two-timescale is the better-fit model have either  $S_i^2$  or  $S_f^2$  close to one in the corresponding three-timescale model, indicating very little motional contribution from the intermediate or fast motion. Because the contributions of one of the three correlation times are minimized, the model is reduced to a form that is very similar to the two-timescale model. Also, the amplitudes and correlation times of the remaining motions are very similar to those in the two-timescale models (see Figure 16 and SI Figure 10). These correlations first indicate that use of the bootstrap method to evaluate error on experiment parameters, and subsequent usage of those errors to evaluate  $\chi^2$  via (20), gives reliable evaluation of model quality. Also, it allows us to rely only on the three-timescale model, since it results in a fit that is similar to the two-timescale model where the AIC parameter favors that model. A side effect of the minimal contribution of one of the motions to the three-timescale model is that it can cause a sharp increase in the error of the corresponding correlation time, since one must be able to measure significant changes in the experimental parameters to be able to accurately characterize the correlation time.

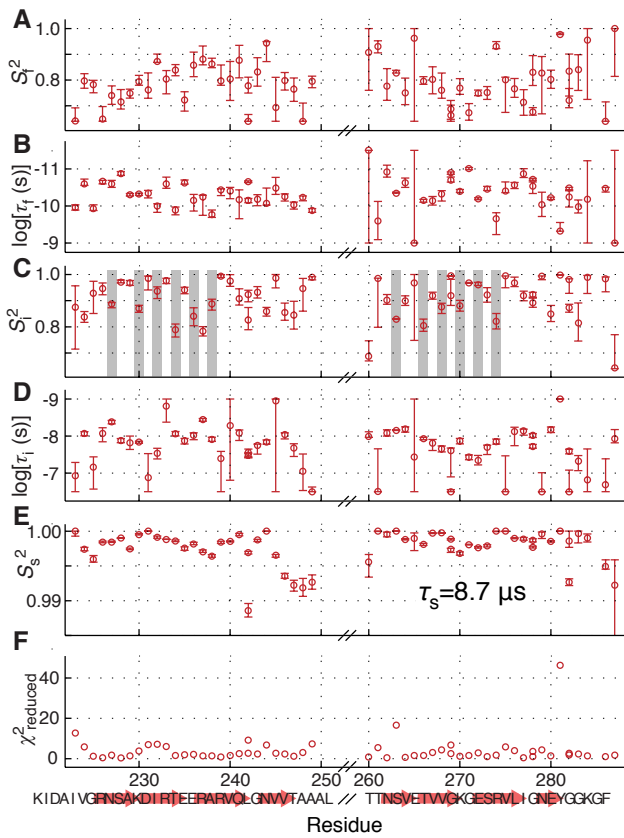


**Figure 13** Fit parameters for  $^1\text{H}\alpha$ - $^{13}\text{C}\alpha$  dynamics using a three-timescale model. (A) gives the residue specific fast motional amplitude ( $S_f^2$ ). (B) gives the fast motional timescale, plotted logarithmically. (C) and (D) give the intermediate motional amplitude ( $S_i^2$ ) and timescale ( $\tau_i$ ), respectively. In (C), we highlight fibril core residues pointing outward in grey (excluding those between  $\beta$ -sheets- see Figure 1). (E) gives the slow motional amplitude ( $S_s^2$ ), using a correlation time of  $\tau_s = 8.7 \mu\text{s}$ . (D) gives the reduced- $\chi^2$  of the fit. (A) – (E) show error bars, which approximate a 68% confidence interval for the parameter



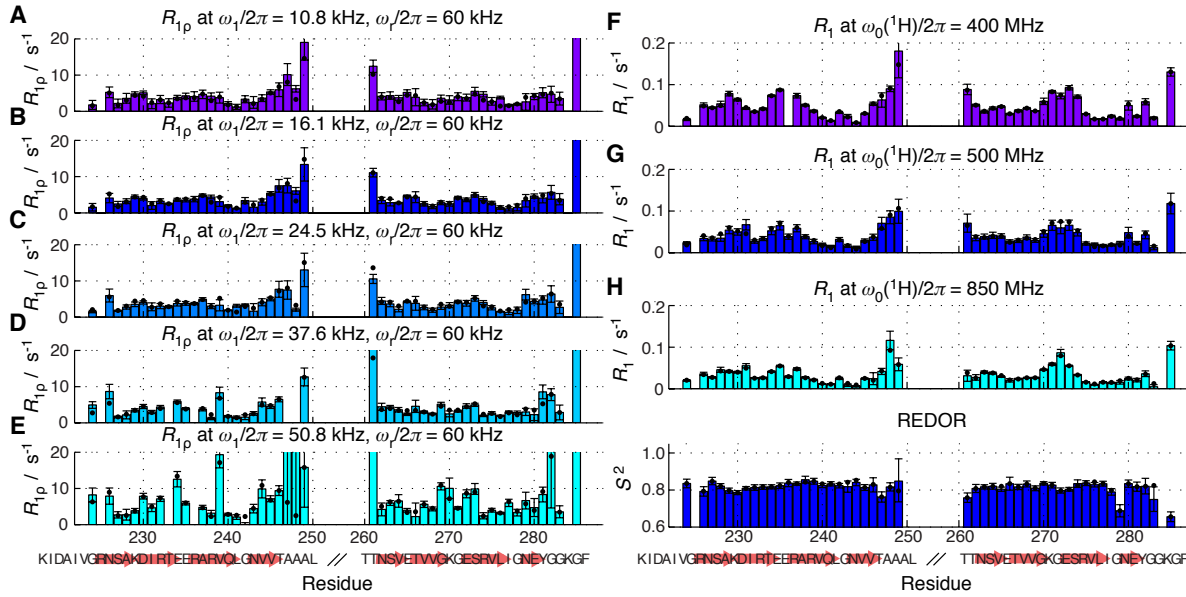


**Figure 14** Experimental parameters for  $^1H-^{15}N$  dynamics fitted to a three-timescale model. (A) – (E) give measured  $R_{1p}$  for different spin-locking strengths (bars), versus values calculated from the fitted model (black dots). (F) – (H) give  $R_1$  measurements and calculated values for different magnetic fields. (I) gives measured versus calculated  $S^2$ , measured with shifted REDOR. All measurements also include error bars, indicating one standard deviation on the measurement data, determined via bootstrapping

The results of fitting of relaxation data can depend critically on the model chosen. For example, when fitting  $^1H\alpha-^{13}C\alpha$  data to a three-timescale model, we note that a trend emerges: the  $S_i^2$  is correlated to the position of the side-chain, where residues that point into the fibril core have higher values of  $S_i^2$  (less motion) and those that point outwards towards the solvent have lower values (more motion). Interestingly, when  $^{13}C\alpha$  data is fitted to a two-timescale model, the same trend emerges, but for values of  $S_s^2$ , which is assumed to be a global motion, as shown in Figure 16. This represents a critical failure of model-free fitting: a motion that is residue-dependent becomes part of the fit of a global motion. A model that is too simple can easily mix two separate motions into one timescale of the model, yielding data that is impossible to interpret reasonably. A similar problem arises when analyzing  $^1H-^{15}N$  dynamics with only a two-timescale model, where most of the nanosecond range motion is omitted entirely from the fit (see SI Figure 10). Both situations demonstrate that determination of the best model via statistical tests is important. However even then, a smaller or lower quality data set may not have the information content to satisfy a more complex model, and so statistical tests would indicate a simpler model is a better fit. This does not mean that the simpler model adequately describes the dynamic behavior, only that the data is insufficient to support a more complex model. This can result in a fit that combines physically distinct

motions into a single motion and correlation time. Then the physical meaning of those motions may be obscured and the resulting fit parameters can be distorted.

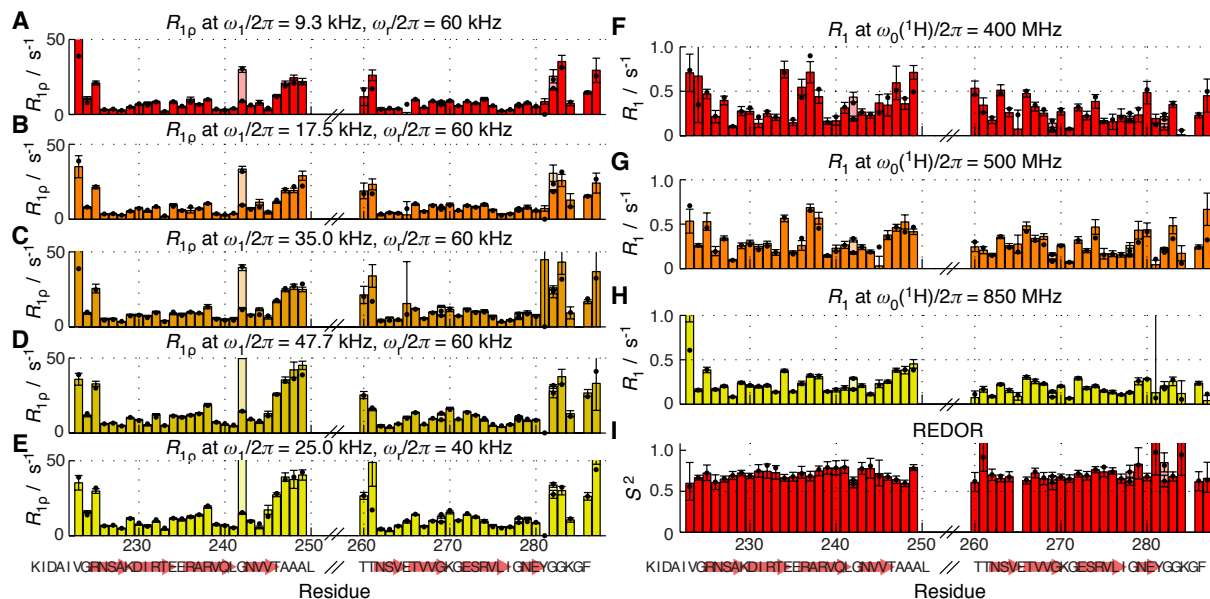


**Figure 15** Experimental parameters for  $^1\text{H}\alpha$ - $^{13}\text{C}\alpha$  dynamics fitted to a three-timescale model. (A) – (E) give measured  $R_{1\rho}$  for different spin-locking strengths and MAS frequencies (bars), versus values calculated from the fitted model (black dots). (F) – (H) give  $R_1$  measurements and calculated values for different magnetic fields. (I) gives measured versus calculated  $S^2$ . All measurements also include error bars, indicating one standard deviation on the measurement data, determined via bootstrapping

Our analysis shows a discrepancy in the best-fit slow correlation times for the analysis of  $^{15}\text{N}$  and  $^{13}\text{C}\alpha$  data, yielding correlation times of 14.7  $\mu\text{s}$  and 8.7  $\mu\text{s}$ , respectively. Although not orders of magnitude apart, the difference is surprising since we postulate that a single, global motion is responsible for the measurement of a microsecond timescale, and so ideally the correlation times would be in full agreement. One potential reason for the difference is that we do not fully account for coherent effects in  $R_{1\rho}$  measurements. We do note that, in particular for  $^{13}\text{C}\alpha$  data, coherent effects are expected to produce notably different trends for  $R_{1\rho}$  than motion, as was shown in Figure 8. There,  $R_{1\rho}$  that is calculated as a result of coherent effects ( $^1\text{H}$ -flipping) for spin-lock strengths of 25 kHz and MAS of 40 kHz, and spin-lock strength of 48 kHz and 60 kHz fit poorly to the dynamic model. Therefore, to check that coherent effects are not contributing significantly to our fit of slow motion, we re-fit  $^1\text{H}\alpha$ - $^{13}\text{C}\alpha$  dynamics data while excluding  $R_{1\rho}$  data measured with 25 kHz/40 kHz, and 48 kHz/60 kHz spin-lock/MAS frequencies, and then predict those data points. The result is shown in SI Figure 13, where we see that most points are very well predicted- indicating that the motional model is reasonable and unlikely to be the result of coherent effects on the  $R_{1\rho}$ . An additional

consideration is that since the source of the microsecond motion is not yet clear, it is possible that the model-free approach does not adequately describe it, and so modeling of  $^{13}\text{C}$  versus  $^{15}\text{N}$  slow dynamics could result in slightly different fitted timescales.

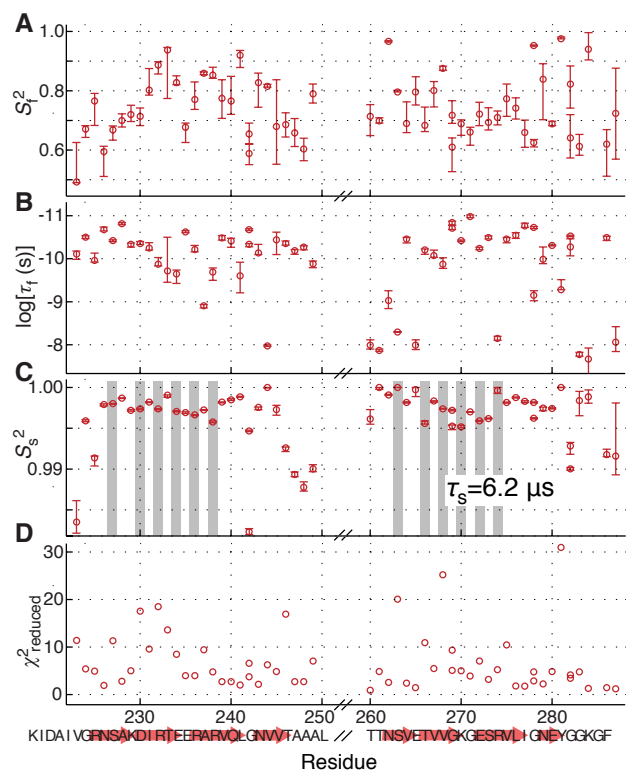


**Figure 16** Fit parameters for  $^1\text{H}\alpha$ - $^{13}\text{C}\alpha$  dynamics using a two-timescale model. (A) gives the residue specific fast motional amplitude ( $S_f^2$ ). (B) gives the fast motional timescale, plotted logarithmically. (C) gives the slow motional amplitude ( $S_s^2$ ), using a correlation time of  $\tau_s = 6.2 \mu\text{s}$ . (D) gives the reduced- $\chi^2$  of the fit. In (C), we highlight fibril core residues pointing outward in grey (excluding those between  $\beta$ -sheets- see Figure 1). (A) – (C) show error bars, which approximate a 68% confidence interval for the parameter

When studying slow motions, it is useful to notice that the slow correlation time of a global motion,  $\tau_s$ , and the site specific slow order parameters,  $S_s^2$  can be fairly well determined only based on  $R_{1\rho}$  data. In this case, one may fit the  $R_{1\rho}$  data while only modeling a single, slow timescale. We do so, and plot the reduced- $\chi^2$  for all residues as a function of  $\tau_s$  in **Figure 17A**, obtaining the best fits for  $\tau_s = 6.2 \mu\text{s}$  for  $^1\text{H}$ - $^{15}\text{N}$  and  $\tau_s = 4.1 \mu\text{s}$  for  $^1\text{H}\alpha$ - $^{13}\text{C}\alpha$  data. These are identical to the rate constants found for the two-timescale model using the full data set. This is because when fitting the full data set for the two-timescale model, the fast timescale is usually in the picosecond range of motion, and so has little effect on the calculated  $R_{1\rho}$ . Similarly, the microsecond motion has no effect on the calculated  $R_1$  values, and since the  $S_s^2$  are very near to one, it also does not contribute significantly to the total order parameter. The resulting residue specific values for  $S_s^2$  are also very similar to those determined using the

two-timescale model, as shown in Figure 18 (see SI Figure 14 for fit of the data). However, there is a systematic overestimation of the  $S_s^2$  determined using only  $R_{1\rho}$  as compared to using the full data set. This is because fast motion reduces the effective dipole coupling, such that the slower motion does not induce as much relaxation, requiring larger motions to account for the same  $R_{1\rho}$  rate constants (see Eq. (1)); when fitting only  $R_{1\rho}$ , one does not determine the faster motions and, therefore, it is impossible to account for the scaling.

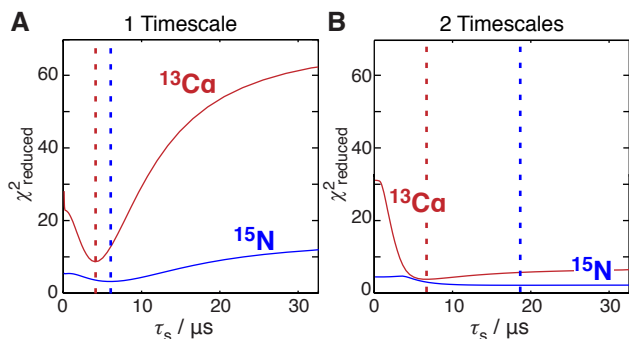


**Figure 17:** Calculation of the slow correlation time,  $\tau_s$ , using only  $R_{1\rho}$  data. (A) shows the reduced- $\chi^2$  calculated for all residues as a function of the slow correlation time for both  $^1\text{H}$ - $^{15}\text{N}$  data and  $^1\text{H}\alpha$ - $^{13}\text{C}\alpha$  data. The model includes only one slow motion. (B) shows the reduced- $\chi^2$  calculated for all residues, but the model includes both a slow timescale, and an intermediate timescale. The correlation times and order parameters are not fitted for the intermediate timescale- only a contribution to the  $R_{1\rho}$  from intermediate timescale motion is fitted, which is independent of MAS and spin-lock frequency.

Alternatively,  $R_{1\rho}$  values may be fitted to a slow timescale, and an intermediate (nanosecond) timescale. In this case, the contribution of the intermediate timescale to  $R_{1\rho}$  will be the same for all experimental conditions (see Eqs. (1), (5), and (6)), where the dependence of  $R_{1\rho}$  on the MAS and field strength vanishes for sufficiently short correlation times). Then, it will be impossible to characterize the intermediate timescale with  $S_i^2$  and  $\tau_i$ , but the data can nonetheless be fitted with a constant contribution to all  $R_{1\rho}$  measurements for a given residue due to the intermediate timescale motion ( $R_{1\rho}$  offset). We perform this fit, for various values of  $\tau_s$ , and plot the reduced- $\chi^2$  for each in **Figure 17B**, obtaining best fits for  $\tau_s = 18.5 \mu\text{s}$  for  $^1\text{H}$ - $^{15}\text{N}$  and  $\tau_s = 7.0 \mu\text{s}$  for  $^1\text{H}\alpha$ - $^{13}\text{C}\alpha$  motion. The values are very similar to those found for the three-timescale model, although no longer identical (as compared to  $14.7 \mu\text{s}$  and  $8.7 \mu\text{s}$ ). Values of  $S_s^2$  are also similar, although again biased because scaling of the relaxation by faster motions is not accounted for (see SI Figure 15, and SI Figure 16 for fit of the data). Some differences emerge because the intermediate (nanosecond) motion affects all measured parameters ( $R_1$ ,  $R_{1\rho}$ , and  $S^2$ ). Then, influence of  $R_1$  and  $S^2$  on the intermediate motion affects its contribution to

calculation of  $R_{1\rho}$ , resulting in minor changes to the calculated slow correlation time. Ultimately, the extraction of information on slow, microsecond motion from only  $R_{1\rho}$  data is complicated by contributions to  $R_{1\rho}$  from intermediate motion. However, if the slow motion is global, the fact that all residues can be fitted to one correlation time makes a reasonable analysis possible, whereas determination of residue-specific slow correlation times and amplitudes along with contributions to  $R_{1\rho}$  from intermediate timescale motion would be extremely difficult.

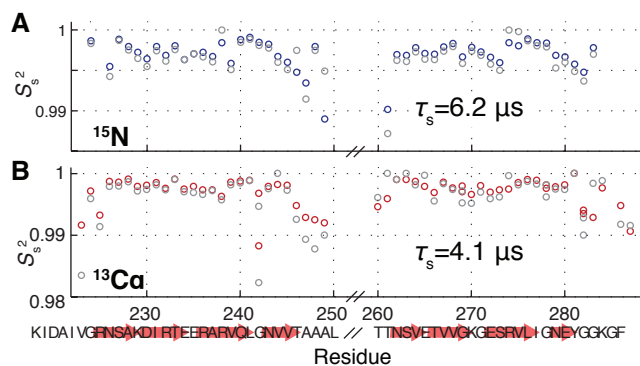


**Figure 18:**  $S_s^2$  determined for  $^1\text{H}-^{15}\text{N}$  and  $^1\text{H}\alpha-^{13}\text{C}\alpha$  motion using only  $R_{1\rho}$  data. Colored dots show  $S_s^2$  for which only  $R_{1\rho}$  data was fitted to a single, slow motion, with a correlation time of  $6.2\ \mu\text{s}$  for  $^{15}\text{N}$  data and  $4.1\ \mu\text{s}$  for  $^{13}\text{C}\alpha$  data. Grey dots show  $S_s^2$  determined while fitting the full data set to a two-timescale model, showing that usually fitting to the full data set predicts a lower  $S_s^2$  (larger motion).

## 5 Conclusions

The combined use of  $R_1$ ,  $R_{1\rho}$ , and  $S^2$  data for both  $^1\text{H}\alpha-^{13}\text{C}\alpha$  and  $^1\text{H}-^{15}\text{N}$  has been shown to be a powerful addition to dynamics analysis, and allows the descriptions of the dynamics by three timescales of motion, representative of a slow, global motion, intermediate, and fast motion. Measurement of similar slow motion on both nuclei gives further evidence of the presence of a slow motion, whereas nanosecond and picosecond motions showed differences in trends between  $^1\text{H}\alpha-^{13}\text{C}\alpha$  and  $^1\text{H}-^{15}\text{N}$ , indicating that they provide information on different motions. Of course a three-timescale model is still a rather crude description of the complex dynamics of a protein fibril but the three-timescale fit of both  $^1\text{H}-^{15}\text{N}$  and  $^1\text{H}\alpha-^{13}\text{C}\alpha$  motion pushes the limits of the information content of our dynamics data, although is supported by statistics that show that most residues are better fit with a three-timescale model. Our ability to separate three timescales relies heavily on the fact that it was possible to use a single slow-motion correlation time for all residues, reducing the number of parameters being fitted for each residue.

Having a sufficiently complex model to represent the protein motion is critical. In our case, if only two timescales are used to describe  $^1\text{H}\alpha-^{13}\text{C}\alpha$  motion, then slow and intermediate

motion of  $^1\text{H}\alpha$ - $^{13}\text{C}\alpha$  are interpreted as a single motion, and the physical meaning of both motions becomes highly convoluted, since features of both motions are mixed together into a single parameter set. Similarly, when  $^1\text{H}$ - $^{15}\text{N}$  motion is fitted to a two-timescale model, most nanosecond timescale motion is excluded from the resulting model. One may use statistical tests to verify that a more complex model is supported by the data, as we have done with the AIC parameter, but when the statistical test supports usage of a simpler model, it does not prove that the real motion is well described by the simpler model. It then may be necessary to improve the experimental data set to obtain a good description of the real motion. In our case, most of the residues for which the simpler, two-timescale model was favored by the AIC parameter, the three-timescale model also indicated that one motion contributed only slightly to the dynamics behavior, giving good agreement between results of model fitting and statistical analysis. Of course similar errors may be introduced into our three-timescale model as additional timescales certainly exist but cannot be characterized by present day experiments.

We were able to obtain evidence of global motion in the HET-s fibril, with similar slow correlation times ( $\tau_s$ ) for both  $^1\text{H}$ - $^{15}\text{N}$  and  $^1\text{H}\alpha$ - $^{13}\text{C}\alpha$  models. Fitting of slow motion on both nuclei with similar correlation times shows that the slow motion is unlikely to be an experimental artifact. The ability to make a direct comparison of the slow motion relies on the fact that it is a global motion, and so should be highly correlated. Still, combining data from multiple nuclei can be worthwhile, as shown by Lamley et al., where the motion of the peptide plane can be modeled from combined  $^{15}\text{N}$  and  $^{13}\text{C}'$  (backbone carbonyl) data (Lamley et al. 2015). This is not true for  $^1\text{H}$ - $^{15}\text{N}$  and  $^1\text{H}\alpha$ - $^{13}\text{C}\alpha$  that is not global, since the bonds to  $^{13}\text{C}\alpha$  do not lie in the peptide plane. Therefore, whereas combination of  $^{15}\text{N}$  relaxation and  $^{13}\text{C}'$  motion may be used to more accurately characterize the concerted peptide plane motion, combination of  $^{15}\text{N}$  and  $^{13}\text{C}\alpha$  relaxation can highlight different motions. Of course, all nuclei can be combined to investigate global motions, and it is possible for a single local motion (several nuclei) to be observed on both the  $^{15}\text{N}$  and  $^{13}\text{C}\alpha$  nuclei, although in our study,  $^{15}\text{N}$  and  $^{13}\text{C}\alpha$  motions were not strongly correlated.

If motional parameters acquired from different nuclei are compared as a means for model verification, or analyzed in concert, it becomes critical that the model used to calculate  $R_{1\rho}$  is correct. Approximations in the  $R_{1\rho}$  calculation can still yield qualitative results for a single type of nucleus but the degree of error will vary for different types of nuclei. Therefore, one should rely on more accurate simulations rather than Redfield-theory based methods for slow motions particularly when multiple nuclei are being used. Furthermore, it is important to

account for magnetization decay induced by  $^1\text{H}$  inversion, both in order to maintain agreement between different nuclei and additionally to avoid misinterpreting such  $^1\text{H}$  inversion induced magnetization decay as slow motion. Although many of the errors that we have corrected here are relatively small, the errors can accumulate, making the additional effort required for an accurate analysis worthwhile.

## References

- Abdullah A, Deris S, Anwar S, Arjunan SNV (2013) An Evolutionary Firefly Algorithm for the Estimation of Nonlinear Biological Model Parameters. *PloS One* 8:e56310
- Abergel D, Palmer AGI (2003) On the Use of the Stochastic Liouville Equation in Nuclear Magnetic Resonance: Application to  $R_1'$  Relaxation in the Presence of Exchange. *Concepts Magn Reson A* 19A:134-148
- Agarwal V, Penzel S, Szekely K, Cadalbert R, Testori E, Oss A, Past J, Samoson A, Ernst M, Böckmann A, Meier BH (2014) De Novo 3D Structure Determination from Sub-milligram Protein Samples by Solid-State 100 kHz MAS NMR Spectroscopy. *Angew Chem Int Ed* 53:12253-12256
- Akaike H (1974) A New Look at the Statistical Model Identification. *IEEE T Automat Contr* 19:716-723
- Allerhand A, Doddrell D, Glushko V, Cochran DW, Wenkert E, Lawson PJ, Gurd FRN (1971) Conformation and Segmental Motion of Native and Denatured Ribonuclease A in Solution. Application of Natural-Abundance Carbon-13 Partially Relaxed Fourier Transform Nuclear Magnetic Resonance. *J Am Chem Soc* 93:544-546
- Asami S, Porter JR, Lange O, Reif B (2015) Access to  $\text{C}\alpha$  Backbone Dynamics of Biological Solids by  $^{13}\text{C}$   $T_1$  Relaxation and Molecular Dynamics Simulation. *J Am Chem Soc* 137:1094-1100
- Asami S, Schmieder P, Reif B (2010) High Resolution  $^1\text{H}$ -Detected Solid-State NMR Spectroscopy of Protein Aliphatic Resonances: Access to Tertiary Structure Information. *J Am Chem Soc* 132:15133-15135
- Asami S, Szekely K, Schanda P, Meier BH, Reif B (2012) Optimal degree of protonation for  $^1\text{H}$  detection of aliphatic sites in randomly deuterated proteins as a function of the MAS frequency. *J Biomol NMR* 54:155-168
- Bak M, Rasmussen JT, Nielsen NC (2000) SIMPSON: A General Simulation Program for Solid-State NMR Spectroscopy. *J Magn Res* 147:296-330
- Balguerie A, Dos Reis S, Ritter C, Chaignepain S, Bénédicte C-S, Forge V, Bathany K, Lascu I, Schmitter J-M, Riek R, Saupe SJ (2003) Domain organization and structure±function relationship of the HET-s prion protein of *Podospora anserina*. *EMBO J* 22:2071-2081
- Böckmann A, Gardiennet C, Verel R, Hunkeler A, Loquet A, Pintacuda G, Emsley L, Meier BH, Lesage A (2009) Characterization of different water pools in solid-state NMR protein samples. *J Biomol NMR* 45:319-327
- Chevelkov V, Diehl A, Reif B (2007a) Quantitative measurement of differential  $^{15}\text{N}$ - $^1\text{H}$   $T_2$  relaxation rates in a perdeuterated protein by MAS solid-state NMR spectroscopy. *Magn Reson Chem* 45:S156-S160
- Chevelkov V, Fink U, Reif B (2009) Quantitative analysis of backbone motion in proteins using MAS solid-state NMR spectroscopy. *J Biomol NMR* 45:197-206

- Chevelkov V, Zhuravleva AV, Xue Y, Reif B, Skrynnikov N (2007b) Combined Analysis of <sup>15</sup>N Relaxation Data from Solid- and Solution-State NMR Spectroscopy. *J Am Chem Soc* 129:12594-12595
- Clifford AA (1973) *Multivariate error analysis: a handbook of error propagation and calculation in many-parameter systems*. Wiley, New York, NY
- Clore GM, Szabo A, Bax A, Kay LE, Driscoll PC, Gronenborn AM (1990) Deviations from the Simple Two-Parameter Model-Free Approach to the Interpretation of Nitrogen-15 Nuclear Magnetic Relaxation of Proteins. *J Am Chem Soc* 112:4989-4991
- Efron B, Tibshirani R (1993) *An Introduction to the Bootstrap*. CRC Press, Boca Raton, FL, USA
- Emsley L, Bodenhausen G (1992) Optimization of Shaped Selective Pulses for NMR Using a Quaternion Description of Their Overall Propagators. *J Magn Res* 97:135-148
- Ernst M, Meier BH (1998) Spin Diffusion in Solids. In: Ando I, Asakura T (eds) *Solid State NMR of Polymers*, vol 84. Elsevier, pp 83-121
- Giraud N, Blackledge M, Böckmann A, Emsley L (2007) The influence of nitrogen-15 proton-driven spin diffusion on the measurement of nitrogen-15 longitudinal relaxation time. *J Magn Res* 184:51-61
- Giraud N, Blackledge M, Goldman M, Böckmann A, Lesage A, Penin F, Emsley L (2005) Quantitative Analysis of Backbone Dynamics in a Crystalline Protein from Nitrogen-15 Spin-Lattice Relaxation. *J Am Chem Soc* 127:18190-18201
- Glass NL, Kaneko I (2003) Fatal Attraction: Nonself Recognition and Heterokaryon Incompatibility in Filamentous Fungi. *Eukaryot Cell* 2:1-8
- Good DB, Wang S, Ward ME, Struppe J, Brown LS, Lewandowski JR, Ladizhansky V (2014) Conformational Dynamics of a Seven Transmembrane Helical Protein Anabaena Sensory Rhodopsin Probed by Solid-State NMR. *J Am Chem Soc* 136:2833-2842
- Grommek A, Meier BH, Ernst M (2006) Distance information from proton-driven spin diffusion under MAS. *Chem Phys Lett* 427:404-409
- Gullion T, Baker DB, Conradi MS (1990) New, Compensated Carr-Purcell Sequences. *J Magn Res* 89:479-484
- Gullion T, Schaefer J (1989a) Detection of Weak Heteronuclear Dipolar Recoupling by Rotational-Echo Double-Resonance Nuclear Magnetic Resonance. *Adv Magn Res* 13:57-83
- Gullion T, Schaefer J (1989b) Rotational-Echo Double-Resonance NMR. *J Magn Res* 81:196-200
- Haeberlen U, Waugh JS (1969) Spin-Lattice Relaxation in Periodically Perturbed Systems. *Phys Rev* 185:420-429
- Haller JD, Schanda P (2013) Amplitudes and time scales of picosecond-to-microsecond motion in proteins studied by solid-state NMR: a critical evaluation of experimental approaches and application to crystalline ubiquitin. *J Biomol NMR* 57:263-280
- Hediger S, Meier BH, Ernst RR (1995) Adiabatic passage Hartmann-Hahn cross polarization in NMR under magic angle sample spinning. *Chem Phys Lett* 240:449-456
- Henzler-Wildman K, Kern D (2007) Dynamic personalities of proteins. *Nature* 450:964-972
- Herrmann US, Schütz AK, Shirani H, Huang D, Saban D, Nuvolone M, Li B, Ballmer B, Åslund AKO, Mason JJ, Rushing E, Budka H, Nyström S, Hammarström P, Böckmann A, Caffisch A, Meier BH, Nilsson KPR, Hornemann S, Aguzzi A (2015) Structure-based drug design identifies polythiophenes as antiprion compounds. *Sci Transl Med* 7:299ra123
- Hou G, Paramasivam S, Byeon I-JL, Gronenborn AM, Polenova T (2010) Determination of relative tensor orientations by c-encoded chemical shift anisotropy/heteronuclear dipolar



- coupling 3D NMR spectroscopy in biological solids. *Phys Chem Chem Phys* 12:14873-14883
- Jaroniec C, Tounge B, Rienstra C, Herzfeld J, Griffin R (2000) Recoupling of heteronuclear dipolar interactions with rotational-echo double-resonance at high magic-angle spinning frequencies. *J Magn Reson* 146:132-139
- Jaroniec CP, Tounge BA, Herzfeld J, Griffin RG (2001) Frequency Selective Heteronuclear Dipolar Recoupling in Rotating Solids: Accurate  $^{13}\text{C}$ - $^{15}\text{N}$  Distance Measurements in Uniformly  $^{13}\text{C}$ ,  $^{15}\text{N}$ -labeled Peptides. *J Am Chem Soc* 123:3507-3519
- Jeener J, Meier BH, Bachman P, Ernst RR (1979) Investigation of exchange processes by two-dimensional NMR spectroscopy. *J Chem Phys* 71:4546-4553
- Kaiser R (1963) Use of the Nuclear Overhauser Effect in the Analysis of High - Resolution Nuclear Magnetic Resonance Spectra. *J Chem Phys* 39:2435-2442
- Krushelnitsky A, Zinkevich T, Reichert D, Chevelkov V, Reif B (2010) Microsecond Time Scale Mobility in a Solid Protein As Studied by the  $^{15}\text{N}$  R1G Site-Specific NMR Relaxation Rates. *J Am Chem Soc* 132:11850-11853
- Kubo R (1963) Stochastic Liouville Equations. *J Math Phys* 4:174-183
- Kurbanov R, Zinkevich T, Krushelnitsky A (2011) The nuclear magnetic resonance relaxation data analysis in solids: General R 1/R 1 equations and the model-free approach. *J Chem Phys* 135:184104 (184101-184109)
- Lamley JM, Lougher MJ, Sass HJ, Rogowski M, Grzesiek S, Lewandowski JR (2015) Unraveling the complexity of protein backbone dynamics with combined  $^{13}\text{C}$  and  $^{15}\text{N}$  solid-state NMR relaxation measurements. *Phys Chem Chem Phys* 17:21997-22008
- Lange A, Gattin Z, Van Melckebeke H, Wasmer C, Soragni A, Gunsteren WF, Meier BH (2009) A Combined Solid-State NMR and MD Characterization of the Stability and Dynamics of the HET-s(218-289) Prion in its Amyloid Conformation. *ChemBioChem* 10:1657-1665
- Lewandowski JR, Sein J, Sass HJ, Grzesiek S, Blackledge M, Emsley L (2010) Measurement of Site-Specific  $^{13}\text{C}$  Spin-Lattice Relaxation in a Crystalline Protein. *J Am Chem Soc* 132:8252-8254
- Lipari G, Szabo A (1982) Model-free approach to the interpretation of nuclear magnetic resonance relaxation in macromolecules. 1. Theory and range of validity. *J Am Chem Soc* 104:4546-4559
- Lundström P, Hansen DF, Vallurupalli P, Kay LE (2009) Accurate Measurement of Alpha Proton Chemical Shifts of Excited Protein States by Relaxation Dispersion NMR Spectroscopy. *J Am Chem Soc* 131:1915-1926
- Ma P, Haller JD, Zajakala J, Macek P, Siversten AC, Willbold D, Boisbouvier J, Schanda P (2014) Probing Transient Conformational States of Proteins by Solid-State R1p Relaxation-Dispersion NMR Spectroscopy. *Angew Chem Int Ed* 53:4312-4317
- Ma P, Xue Y, Coquelle N, Haller JD, Yuwen T, Ayala I, Mikhailovskii O, Willbold D, Colletier J-P, Skrynnikov NR, Schanda P (2015) Observing the overall rocking motion of a protein in crystal. *Nat Commun* 6:8361
- McConnell HM (1958) Reaction Rates by Nuclear Magnetic Resonance. *J Chem Phys* 28:430-431
- Mollica L, Baias M, Lewandowski JR, Wylie BJ, Sperling LJ, Rienstra CM, Emsley L, Blackledge M (2012) Atomic-Resolution Structural Dynamics in Crystalline Proteins from NMR and Molecular Simulation. *J Phys Chem Lett* 3:3657-3662
- Nielsen NC, Bildsøe H, Jakobsen HJ (1994) Double-quantum homonuclear rotary resonance: Efficient dipolar recovery in magic-angle spinning nuclear magnetic resonance. *J Chem Phys* 101:1805-1812

- Oas TG, Griffin RG, Levitt MH (1988) Rotary resonance recoupling of dipolar interactions in solid - state nuclear magnetic resonance spectroscopy. *J Chem Phys* 89:692-695
- Redfield AG (1957) On the Theory of Relaxation Processes. *IBM J Res Dev* 1:19-31
- Saupe SJ (2000) Molecular Genetics of Heterokaryon Incompatibility in Filamentous Ascomycetes. *Microbiol Mol Biol Rev* 64:489-502
- Schanda P, Meier BH, Ernst M (2010) Quantitative Analysis of Protein Backbone Dynamics in Microcrystalline Ubiquitin by Solid-State NMR Spectroscopy. *J Am Chem Soc* 132:15957-15967
- Schanda P, Meier BH, Ernst M (2011) Accurate measurement of one-bond H-X heteronuclear dipolar couplings in MAS solid-state NMR. *J Magn Res* 210:246-259
- Schneider DJ, Freed JH (1989) Spin Relaxation and Motional Dynamics. *Adv Chem Phys* 73:387-527
- Schütz AK, Soragni A, Hornemann S, Aguzzi A, Ernst M, Böckmann A, Meier BH (2011) The Amyloid–Congo Red Interface at Atomic Resolution. *Angew Chem Int Ed* 50:5956-5960
- Siemer AB, Ritter C, Steinmetz MO, Ernst M, Riek R, Meier BH (2006) <sup>13</sup>C, <sup>15</sup>N Resonance assignment of parts of the HET-s prion protein in its amyloid form. *J Biomol NMR* 34:75-87
- Skrynnikov N (2007) Asymmetric doublets in MAS NMR: coherent and incoherent mechanisms. *Magn Reson Chem* 45:S161
- Solomon I (1955) Relaxation Processes in a System of Two Spins. *Physical Review Phys Rev PR* 99:559
- Takegoshi K, Nakamura S, Terao T (2001) <sup>13</sup>C-1H dipolar-assisted rotational resonance in magic-angle spinning NMR. *Chem Phys Lett* 344:631-637
- Takegoshi K, Nakamura S, Terao T (2003) <sup>13</sup>C – 1H dipolar-driven <sup>13</sup>C – <sup>13</sup>C recoupling without <sup>13</sup>C rf irradiation in nuclear magnetic resonance of rotating solids. *J Chem Phys* 118:2325-2341
- The MathWorks I (2013) MATLAB, 2013b edn., Natick, Massachusetts, USA
- Torchia DA, Szabo A (1982) Spin-Lattice Relaxation in Solids. *J Magn Res* 49:107-121
- Van Melckebeke H, Schanda P, Gath J, Wasmer C, Verel R, Lange A, Meier BH, Böckmann A (2011) Probing Water Accessibility in HET-s(218–289) Amyloid Fibrils by Solid-State NMR. *J Mol Biol* 405:765-772
- Van Melckebeke H, Wasmer C, Lange A, AB E, Loquet A, Böckmann A, Meier BH (2010) Atomic-Resolution Three-Dimensional Structure of HET-s(218-289) Amyloid Fibrils by Solid-State NMR Spectroscopy. *J Am Chem Soc* 132:13765-13775
- Wasmer C, Lange A, Van Melckebeke H, Siemer AB, Riek R, Meier BH (2008) Amyloid Fibrils of the HET-s(218-289) Prion Form a  $\beta$  Solenoid with a Triangular Hydrophobic Core. *Science* 319:1523-1526
- Wittebort RJ, Szabo A (1978) Theory of NMR relaxation in macromolecules: Restricted diffusion and jump models for multiple internal rotations in amino acid side chains. *J Chem Phys* 69:1722-1736
- Wylie BJ, Franks WT, Rienstra CM (2006) Determinations of <sup>15</sup>N Chemical Shift Anisotropy Magnitudes in a Uniformly <sup>15</sup>N,<sup>13</sup>C-Labeled Microcrystalline Protein by Three-Dimensional Magic-Angle Spinning Nuclear Magnetic Resonance Spectroscopy. *J Phys Chem B* 110:10926-10936
- Xue Y, Skrynnikov N (2014) Ensemble MD simulations restrained via crystallographic data: Accurate structure leads to accurate dynamics. *Protein Sci* 23:488-507
- Zhou DH, Rienstra CM (2008) High-performance solvent suppression for proton detected solid-state NMR. *J Magn Res* 192:167-172

Zinkevich T, Chevelkov V, Reif B, Saalwächter K, Krushelnitsky A (2013) Internal protein dynamics on ps to us timescales as studied by multi-frequency  $^{15}\text{N}$  solid-state NMR relaxation. *J Biomol NMR* 57:219-235